ISSN 2409–5613 (print)
ISSN 2411–1414 (online)

Chimica
Techno
Acta

2019. Vol. 6. N 3

cta.urfu.ru

Chimica Techno Acta

2019 | Vol. 6 | № 3

Scientific and Technical Journal
Established in 2014
Published four times per year

Chimica Techno Acta
© Ural Federal University, 2019

Founded by Ural Federal
University named after the first
President of Russia B. N. Yeltsin
19, Mira St., Ekaterinburg,
620002, Russia

Editorial Board
Editor-in-Chief
A. Yu. Zuev (Ekaterinburg, Russia)
Managing Editor
T. A. Pospelova (Ekaterinburg, Russia)
Copyeditor
V. V. Sereda (Ekaterinburg, Russia)
Editors
E. V. Antipov (Moscow, Russia)
V. A. Cherepanov (Ekaterinburg, Russia)
Zh.-J. Fan (Tianjin, China)
V. V. Gusarov (Saint Petersburg, Russia)
V. V. Kharton (Chernogolovka, Russia)
A. A. Mikhailovsky (Santa Barbara, United States)
V. V. Pankov (Minsk, Belarus)
Sougata Santra (Ekaterinburg, Russia)
N. V. Tarakina (Berlin, Germany)
G. V. Zyryanov (Ekaterinburg, Russia)
D. A. Medvedev (Ekaterinburg, Russia)
P. Tsiakaras (Thessaly, Greece)
S. Song (Guangzhou, China)
Y. Wang (Guangzhou, China)

Chimica Techno Acta

2019 | Vol. 6 | № 3

Научно-технический журнал
Журнал основан в 2014 г.
Выходит четыре раза в год

Chimica Techno Acta
© Уральский федеральный
университет, 2019

Учредитель —
Уральский федеральный
университет
имени первого Президента
России Б. Н. Ельцина
620002, Россия, Екатеринбург,
ул. Мира, 19

Редакционный совет
Главный редактор
А. Ю. Зуев (Екатеринбург, Россия)
Зав. редакцией
Т. А. Поспелова (Екатеринбург, Россия)
Научный редактор
В. В. Середа (Екатеринбург, Россия)
Редакторы
Е. В. Антипов (Москва, Россия)
В. А. Черепанов (Екатеринбург, Россия)
Ж.-Дж. Фан (Тяньцзинь, Китай)
В. В. Гусаров (Санкт-Петербург, Россия)
В. В. Хартон (Черноголовка, Россия)
А. А. Михайловский (Санта-Барбара, США)
В. В. Паньков (Минск, Беларусь)
Согата Сантра (Екатеринбург, Россия)
Н. В. Таракина (Берлин, Германия)
Г. В. Зырянов (Екатеринбург, Россия)
Д. А. Медведев (Екатеринбург, Россия)
П. Циакарас (Фессалия, Греция)
С. Сонг (Гуанчжоу, Китай)
Й. Ванг (Гуанчжоу, Китай)

Graphical Abstracts

CONTENTS/СОДЕРЖАНИЕ

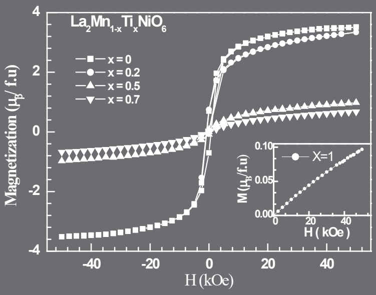

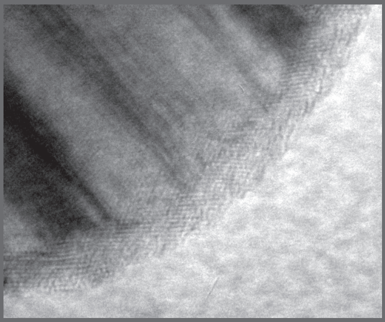

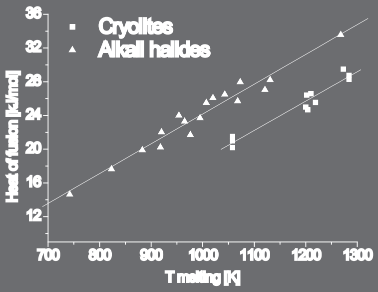

Uma Dutta, Ariful Haque, Md. Motin Seikh
Chimica Techno Acta. 2019. Vol. 6, No. 3. P. 80–92.
ISSN 2409–5613

DOI: 10.15826/chimtech.2019.6.3.01

Uma Dutta, Ariful Haque, Md. Motin Seikh*
Department of Chemistry, Visva-Bharati University,
Santiniketan-731235, West Bengal, India
**E-mail: mdmotin.seikh@visva-bharati.ac.in*

Synthesis, structure and magnetic properties of Ti doped La_2MnNiO_6 double perovskite

We report sol-gel synthesis, structural characterization and magnetic properties of $La_2Mn_{1-x}Ti_xNiO_6$ ($0 \le x \le 1.0$). Ti doping removed the biphasic structure of La_2MnNiO_6 by suppression of rhombohedral structure and all the Ti containing samples crystallized in monoclinic $P2_1/n$ symmetry. La_2MnNiO_6 exhibits multiple magnetic transitions. The high temperature ferromagnetic transition of La_2MnNiO_6 gradually shifted to lower temperatures with increase in Ti doping. La_2TiNiO_6 ($x = 1.0$) does not show any long-range magnetic ordering. The suppression of magnetic transition by Ti doping is ascribed to the destruction of $Mn^{4+} – O – Ni^{2+}$ superexchange interaction. However, the signature of ferromagnetic phase persists up to 70% Ti doping, indicating the robustness of magnetic ordering in La_2MnNiO_6. These results suggest that the addition of Ti^{4+} truncates the ferromagnetic $Mn^{4+} – O – Ni^{2+}$ superexchange path and it likely promotes ferromagnetic cluster formation. The robustness of ferromagnetic state towards Ti substitution compared to the simple perovskite or spinel structure can be attributed to cationic ordering in double perovskite structure. Both the pure and Ti-doped samples exhibit magnetic frustration at lower temperatures due to partial cationic disordering. The absence of long-range ordering in La_2TiNiO_6, unlike La_2TiCoO_6 or Pr_2TiCoO_6, could be related to cationic disordering.

Keywords: double perovskite; ferromagnetic; superexchange interaction; magnetic frustration; cationic disorder; magnetic cluster.

Received: 20.08.2019. Accepted: 11.09.2019. Published: 15.10.2019.

Introduction

Oxides of transition metals with perovskite structure $LnMO_3$ (where Ln is rare earth elements or alkaline earth and M is transition element) exhibit various exotic physical properties related to the correlation between spin, charge, lattice and orbital degrees of freedom [1–3]. These strongly correlated electronic systems show competing electronic and magnetic states. Accordingly, compounds with perovskite structure have most extensively been studied by the physics and chemistry communities due to their magnetic, transport and magnetotransport properties [4]. Presence of second transition metal in the perovskite structure further improves the characteristic features of the so-called double perovskites, $Ln_2MM'O_6$. The important features of double perovskite are cationic ordering, antiphase boundaries and multiple exchange interactions [5–7]. The rock salt ordering with alternate occupancy of octahedra by different metal ions takes place when there is a large size mismatch or the charge difference is greater than 2 [6, 8, 9]. All these are governed by the local electronic configuration of the transition metal ions. Extensive investigations on double perovskites reveal that by virtue of wide M/M' cationic range they exhibit multifunctional properties like insulating, metallic, ferromagnetic, magnetodielectric, multiferroic, etc., which are suitable for various technological applications [10–13].

Among the double perovskites, La_2MnNiO_6 has attracted special attention due to its striking properties such as multiple structures, multiple magnetic ground states, spin frustration and ferromagnetic insulating behaviour near room temperature with giant magnetodielectricity and magnetoresistance [14–19]. La_2MnNiO_6 is reported to crystallize in biphasic nature with rhombohedral ($R\bar{3}c$) and monoclinic ($P2_1/n$) [14, 15, 20–22] or rhombohedral and orthorhombic ($Pbnm$) symmetry [17, 23]. The high temperature synthesized sample is rhombohedral and low temperature one is monoclinic or orthorhombic, whereas for intermediate temperature range it is biphasic [23]. The phase fraction in the sample is also sensitive to the synthesis condition and post annealing treatment [14, 15, 18]. It was reported that the high-temperature phase transforms to $P2_1/n$ phase at low temperature [14]. The magnetic ordering temperatures are different for different phases. The $R\bar{3}c$ phase shows ferromagnetic ordering at relatively higher temperature (~280 K) compared to the $P2_1/n$ or $Pbnm$ phase (~150 K) [16, 17]. The high temperature magnetic phase is governed by $Mn^{4+} – O – Ni^{2+}$, where for low temperature it is $Mn^{3+} – O – Ni^{3+}$ superexchange interactions [15–17, 23, 24]. There is also report on ferromagnetic transition at T_C~100 K in partially disordered sample, which was attributed to the $Mn^{3+} – O – Ni^{3+}$ interaction [15]. Furthermore, there is also appearance of spin glass behaviour in La_2MnNiO_6 associated with the competing interaction between ferromagnetic superexchange and disorder induced antiferromagnetic $Mn^{4+} – O – Mn^{4+}$ and $Ni^{2+} – O – Ni^{2+}$ interactions [15, 18, 25]. This suggests that the cationic disordering suppressed the high temperature ferromagnetic $Mn^{4+} – O – Ni^{2+}$ interaction of perfectly ordered phase. Another extensively studied compound is La_2MnCoO_6 with ferromagnetic T_C~230 K [26]. The double perovskites in which both metal ions are magnetic exhibit ferromagnetic ordering. However, for the ordered perovskite with single magnetic ion the long-range magnetic ordering is antiferromagnetic and the interaction is supersuperexchange with separation of magnetic centres larger than 5 Å [27, 28]. Such interaction also becomes weaker as reflected from the ordering temperatures. The observed T_N values for La_2CoTiO_6 and Pr_2CoTiO_6 are respectively, 15 K and 17 K [28, 29]. Thus, it would be interesting to investigate the ferromagnetic to antiferromagnetic crossover starting from an ordered ferromagnetic system by gradual replacing one magnetic ion by a nonmagnetic one.

In the present studies we have gradually replaced Mn^{4+} in La_2MnNiO_6 by Ti^{4+} to better understand the role of Mn^{4+} in determining the structural and magnetic properties. To the best of our knowledge there is no report in the literature on investigation of Ti doping in La_2MnNiO_6. The ionic radius of Ti^{4+} (0.605 Å) is larger than that for Mn^{4+} (0.530 Å) [30]. In addition, there are other aspects of this substitution. The replacement of magnetic Mn^{4+} by nonmagnetic Ti^{4+} will make magnetic dilution in system, which in turn will truncate the ferromagnetic exchange path. Thus, substitution of Ti^{4+} in La_2MnNiO_6 is expected to rapidly destroy the ferromagnetic state. Furthermore, by considering the retention of cationic ordering it will bring antiferromagnetic supersuperexchange $Ni^{2+} – O – Ti^{4+} – O – Ni^{2+}$ in place of ferromagnetic $Ni^{2+} – O – Mn^{4+} – O – Ni^{2+}$ exchange path. We observed that the ferromagnetic ground state of La_2MnNiO_6 is very robust and it persists up to 70% doping of Ti^{4+}. We did not observe any antiferromagnetic ordering in La_2TiNiO_6 could be due to cationic disordering.

Experimental

Polycrystalline $La_2Mn_{1-x}Ti_xNiO_6$ ($0 \le x \le 1$) samples were prepared by modified sol-gel technique. At first, stoichiometric amounts of metal nitrates (La, Ni) and acetate (Mn) were dissolved in 100 ml double distilled water followed by the addition of about 5 ml concentrated nitric acid to prevent the hydrolysis of the aquated metal ions. In another small beaker stoichiometric amount (1:1) of titanium isopropoxide $[Ti\{OCH(CH_3)_2\}_4]$, and acetyl acetone were mixed and stirred for about several minutes. These two different solutions were mixed in one single beaker and were stirred for about one hour using a magnetic stirrer to get a clear solution. Citric acid was then added to the solution at four times mole ratio of the total metal ions. The final pH of the solution was found to be ~2. The resulting solution was stirred overnight followed by evaporation of solvent at 100 °C to obtain the gel. The obtained gel was dried by increasing the temperature of hotplate to 150 °C to transform the gel into crude precursor. The crude powders were ground thoroughly by using an agate mortar-pestle and calcined at 500 °C for 6 h in air. The final calcination was performed at 700 °C for 6 h in air to achieve the pure phase samples.

The powder X-ray diffraction (PXRD) patterns were registered with a Bruker D8 Advance X-ray diffractometer using Cu Kα radiation ($\lambda = 1.5418$ Å) operating at 40 kV and 40 mA. The PXRD patterns were recorded in the 2θ range of 10–120° using Lynxeye detector (1D mode) with a step size of 0.02° and a dwell time of 1s per step. Iodometric titration of the samples confirms the oxygen stoichiometry fixed to “O_6” within the limit of accuracy ±0.05.

The dc magnetization measurements were performed using a superconducting quantum interference device (SQUID) magnetometer with a variable temperature cryostat (Quantum Design, San Diego, USA). The magnetic ac susceptibility, $\chi_{ac}(T)$ was measured with a PPMS (Quantum Design, San Diego, USA) with the frequency ranging from 10 Hz to 10 kHz. All the magnetic measurements were performed on powder samples putting inside a Teflon capsule.

Results and discussion

The PXRD patterns for all the $La_2Mn_{1-x}Ti_xNiO_6$ (x = 0, 0.2, 0.3, 0.5, 0.7 and 1.0) samples recorded in the 2q-range 10–120° are shown in Fig. 1. All the patterns are refined by Rietveld method using FullProf suit program [31]. The pattern of the parent compound ($x = 0$) La_2MnNiO_6 can only be refined properly by considering a mixed rhombohedral $R\bar{3}c$ and monoclinic $P2_1/n$ phases. The biphasic nature composed of rhombohedral and monoclinic phases for La_2MnNiO_6 sample was reported in the literature by several researchers [14, 15, 18, 32]. However, the phase fraction depends on synthesis condition as well as on post-synthesis annealing treatment. We observed predominant monoclinic phase (80%) over rhombohedral (20%) one for the sol-gel synthesized La_2MnNiO_6 with final heat treatment in air at 700 °C for 6 h. However, all the Ti doped samples can be nicely indexed with monoclinic structure (sp. gr. $P2_1/n$) (Fig. 1). Thus, the Ti doping suppressed the rhombohedral phase of La_2MnNiO_6. The detailed structural and refinement parameters are given in Table 1. From the Table, one can see the systematic increase in cell volume with the increase in Ti^{4+} content as expected for its larger ionic radius compared to that of Mn^{4+} [30]. We observed that the size of NiO_6 octahedra are slightly larger than that of MnO_6 as reported in the literature [33].

Fig. 2 shows the temperature dependent dc-magnetization measured in both the zero field-cooled (ZFC) and field-cooled (FC) protocols under an applied magnetic field of 500 Oe for the temperature range 5–300 K. The magnetization data of $x = 0$ parent phase exhibit ferromagnetic transition (T_C~280 K) just below room temperature (Fig. 2, *a*). One should notice the large thermomagnetic irreversibility between ZFC and FC data branch immediate below T_C~280 K, where ZFC data show a hump. The ZFC data also

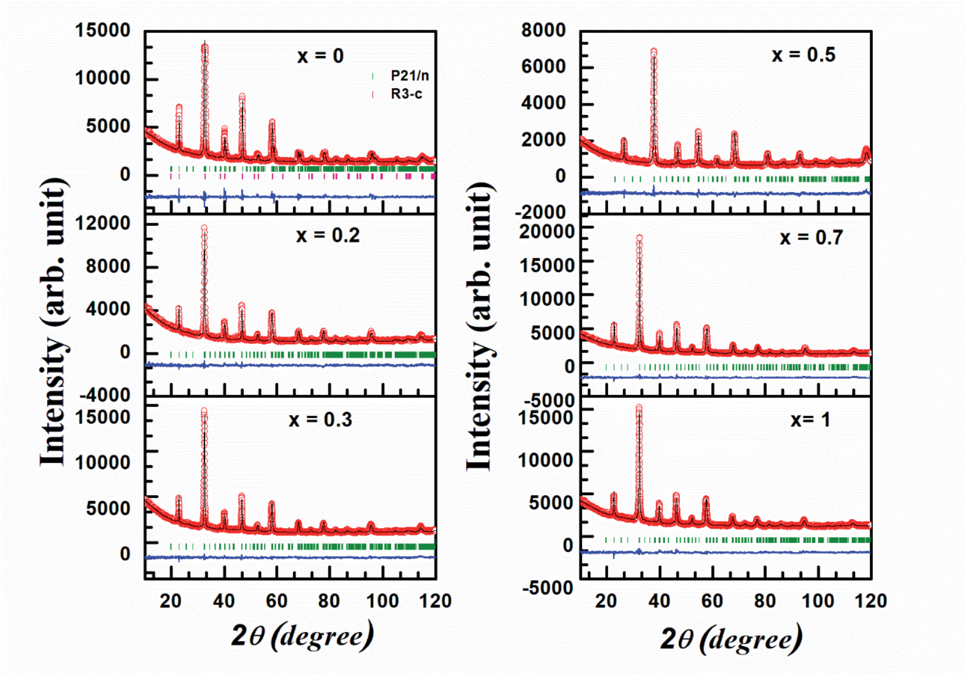

Fig. 1. Powder X-ray diffraction patterns of $La_2Mn_{1-x}Ti_xNiO_6$ ($x = 0$, 0.2, 0.3, 0.5, 0.7 and 1.0). The open red circles, black lines, the bottom blue lines and vertical bars represent the experimental data, calculated pattern, difference curve and Bragg position, respectively

Table 1

Structural refinement parameters for $Ln_2Mn_{1-x}Ti_xNiO_6$ ($0 \le x \le 1$) ceramics

	$x = 0$		$x = 0.2$	$x = 0.3$	$x = 0.5$	$x = 0.7$	$x = 1$
	$P2_1/n$	$R\bar{3}c$					
a (Å)	5.471 (4)	5.516 (2)	5.483 (9)	5.490 (8)	5.511 (8)	5.524 (5)	5.542 (6)
b (Å)	5.493 (3)	5.516 (1)	5.506 (4)	5.513 (6)	5.527 (2)	5.538 (6)	5.553 (6)
c (Å)	7.742 (4)	13.237 (7)	7.760 (4)	7.767 (4)	7.783 (7)	7.802 (5)	7.821 (6)
V (Å^3)	232.72	348.78	234.342	235.156	237.110	238.745	240.778
β (°)	89.369	γ = 120	89.540	89.719	89.720	90.197	90.244
R_B (%)	10.4		13.6	10.8	11.9	9.20	12.3
R_f (%)	14.5		22	23.4	17.0	24.4	26.8
χ^2	2.97		2.63	2.38	2.28	2.26	2.30
Bond length	2×Mn—O$_1$: 1.930 Å 2×Mn—O$_2$: 1.875 Å 2×Mn—O$_3$: 1.956 Å 2×Ni—O$_1$: 1.991 Å 2×Ni—O$_2$: 2.037 Å 2×Ni—O$_3$: 2.007 Å La—O1: 2.318 Å	Mn1—O$_1$: 1.899 Å Ni2—O$_1$: 2.029 Å La1—O1: 3×2.453 Å 6×3.056 Å 3×2.771 Å	×Mn/Ti—O$_1$: 1.934 Å 2×Mn/Ti—O$_2$: 1.885 Å 2×Mn/Ti—O$_3$: 1.906 Å 2×Ni—O$_1$: 2.023 Å 2×Ni—O$_2$: 2.046 Å 2×Ni—O$_3$: 2.033 Å	2×Mn/Ti—O$_1$: 1.935 Å 2×Mn/Ti—O$_2$: 1.888 Å 2×Mn/Ti—O$_3$: 1.909 Å 2×Ni—O$_1$: 2.019 Å 2×Ni—O$_2$: 2.048 Å 2×Ni—O$_3$: 2.035 Å	2×Mn/Ti—O$_1$: 1.939 Å 2×Mn/Ti—O$_2$: 1.894 Å 2×Mn/Ti—O$_3$: 1.914 Å 2×Ni—O$_1$: 2.023 Å 2×Ni—O$_2$: 2.054 Å 2×Ni—O$_3$: 2.041 Å	×Mn/Ti—O$_1$: 1.941 Å 2×Mn/Ti—O$_2$: 1.899 Å 2×Mn/Ti—O$_3$: 1.920 Å 2×Ni—O$_1$: 2.031 Å 2×Ni—O$_2$: 2.058 Å 2×Ni—O$_3$: 2.044 Å	2×Ti—O$_1$: 1.946 Å 2×Ti—O$_2$: 1.905 Å 2×Ti—O$_3$: 1.926 Å 2×Ni—O$_1$: 2.037 Å 2×Ni—O$_2$: 2.064 Å 2×Ni—O$_3$: 2.050 Å

Continuation of table

	$x = 0$		$x = 0.2$	$x = 0.3$	$x = 0.5$	$x = 0.7$	$x = 1$
	$P2_1/n$	$R\bar{3}c$					
			2La—O$_1$: 2.338 Å	La—O$_1$: 2.341 Å	La—O$_1$: 2.349 Å	2La—O$_1$: 2.355 Å	La—O$_1$: 2.367 Å
	La—O$_1$: 3.121 Å		La—O$_1$: 2.721 Å	La—O$_1$: 2.725 Å	La—O$_1$: 2.732 Å	La—O$_1$: 2.737 Å	La—O$_1$: 2.745 Å
	La—O$_1$: 2.723 Å		La—O$_1$: 2.826 Å	La—O$_1$: 2.830 Å	La—O$_1$: 2.838 Å	La—O$_1$: 2.843 Å	La—O$_1$: 2.851 Å
	La—O$_1$: 2.829 Å		La—O$_1$: 3.148 Å	La—O$_1$: 3.152 Å	La—O$_1$: 3.163 Å	La—O$_1$: 3.172 Å	La—O$_1$: 3.182 Å
	La—O$_2$: 2.787 Å		La—O$_2$: 2.476 Å	La—O$_2$: 2.480 Å	La—O$_2$: 2.487 Å	La—O$_2$: 2.500 Å	La—O$_2$: 2.508 Å
	La—O$_2$: 2.729 Å		La—O$_2$: 2.733 Å	La—O$_2$: 2.735 Å	La—O$_2$: 2.742 Å	La—O$_2$: 2.741 Å	La—O$_2$: 2.748 Å
	La—O$_2$: 3.010 Å		La—O$_2$: 2.792 Å	La—O$_2$: 2.793 Å	La—O$_2$: 2.800 Å	La—O$_2$: 2.798 Å	La—O$_2$: 2.805 Å
	La—O$_2$: 2.463 Å		La—O$_2$: 3.024 Å	La—O$_2$: 3.029 Å	La—O$_2$: 3.037 Å	La—O$_2$: 3.052 Å	La—O$_2$: 3.061 Å
	La—O$_3$: 2.713 Å		La—O$_3$: 2.459 Å	La—O$_3$: 2.460 Å	La—O$_3$: 2.467 Å	La—O$_3$: 2.465 Å	La—O$_3$: 2.472 Å
	La—O$_3$: 2.455 Å		La—O$_3$: 2.727 Å	La—O$_3$: 2.732 Å	La—O$_3$: 2.739 Å	La—O$_3$: 2.754 Å	La—O$_3$: 2.762 Å
	La—O$_3$: 2.767 Å		La—O$_3$: 2.780 Å	La—O$_3$: 2.784 Å	La—O$_3$: 2.791 Å	La—O$_3$: 2.805 Å	La—O$_3$: 2.813 Å
	La—O$_3$: 3.057 Å		La—O$_3$: 3.063 Å	La—O$_3$: 3.064 Å	La—O$_3$: 3.072 Å	La—O$_3$: 3.070 Å	La—O$_3$: 3.078 Å
Bond angle (°)	Mn—O$_1$—Ni: 158.44 Mn—O$_2$—Ni: 161.16 Mn—O$_3$—Ni: 162.62	Mn—O—Ni: 162.67	Mn—O$_1$—Ni: 158.31 Mn—O$_2$—Ni: 162.61 Mn—O$_3$—Ni: 161.20	Mn—O$_1$—Ni: 158.3 Mn—O$_2$—Ni: 162.6 Mn—O$_3$—Ni: 161.21	Mn—O$_1$—Ni: 158.26 Mn—O$_2$—Ni: 162.62 Mn—O$_3$—Ni: 161.22	Mn—O$_1$—Ni: 158.27 Mn—O$_2$—Ni: 162.57 Mn—O$_3$—Ni: 161.27	Mn—O$_1$—Ni: 158.25 Mn—O$_2$—Ni: 162.57 Mn—O$_3$—Ni: 161.28

show a second broad hump at low temperature centred around 25 K. Below T_C, FC data show a plateau followed by a definite slope change below 100 K (Fig. 2, *a*). Such magnetic behaviour of the parent phase is in good agreement with the reported data which supports the prevalence three magnetic phases in the temperature window 5–300 K [15–17, 23, 24]. The high temperature T_C is associated with the ferromagnetic $Mn^{4+} – O – Ni^{2+}$ superexchange interaction of cation ordered state. The transition below 100 K ascribed to the $Mn^{3+} – O – Ni^{3+}$ superexchange interaction and lowest temperature anomaly was attributed to the magnetic frustration arising out of partial cationic disordering [15, 18, 25]

For the Ti doped sample with $x = 0.2$, the high temperature magnetic transition largely shifted (~60 K) to lower temperature at T_C~220 K (Fig. 2, *a*). However, the shape of the curve remains similar to that of the parent phase, though the thermomagnetic hysteresis loop shrinks compared to the $x = 0$ sample (Fig. 2, *a*). However, the upturn in magnetization below 100 K is not much shifted for $x = 0.2$ sample compared to $x = 0$. This result indicates that the high temperature magnetic transition associated with $Mn^{4+} – O – Ni^{2+}$ superexchange interaction is largely hampered compared to the $Mn^{3+} – O – Ni^{3+}$ superexchange interaction. This could be due to preferential isovalent substitution effect. Thus, it can be suggested that for 20% Ti doped sample the cationic ordering persists. For $x = 0.5$ the T_C value comes down to 150 K and still one can observe the double humps in ZFC branch data, upturn in FC data below 50 K as well as the thermomagnetic irreversibility (Fig. 2, *b*). It is worth mentioning that the parent phase sample with orthorhombic *Pbnm* or monoclinic $P2_1/n$ structures exhibits ferromagnetic transition at T_C~150 K ascribed to the $Mn^{3+} – O – Ni^{3+}$ superexchange interaction [15–17, 24]. However, we believe that the T_C~150 K for $x = 0.5$ sample is not associated with $Mn^{3+} – O – Ni^{3+}$ superexchange interaction like in parent phase, rather it is related to the weakening of $Mn^{4+} – O – Ni^{2+}$ superexchange interaction due to substitution of nonmagnetic Ti^{4+} in place of Mn^{4+}. The second magnetic phase further shifted below 50 K as indicated by the upturn in FC data in $x = 0.5$ sample (Fig. 2, *b*). This indicates that still there is possible cationic ordering up to 50% Ti doping in La_2MnNiO_6. On further increase in Ti doping to $x = 0.7$, there is only one broad hump in ZFC data around 20 K and FC data show up turn below 100 K (Fig. 2, *b*). This indicates that the high and

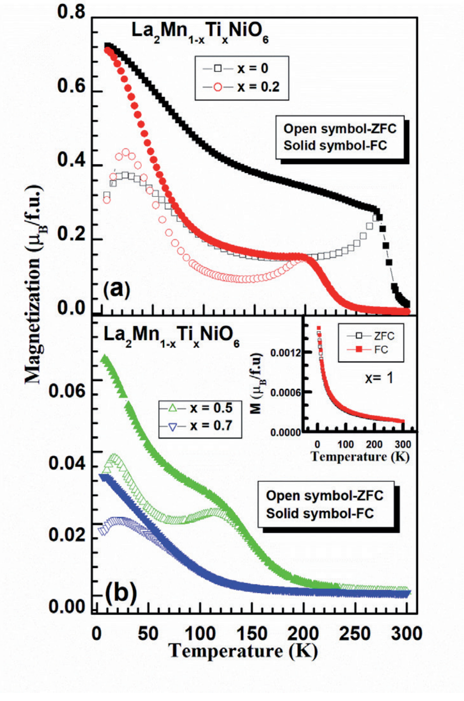

Fig. 2. Temperature dependent dc-magnetization of $La_2Mn_{1-x}Ti_xNiO_6$: *a* — for $x = 0$ and 0.2 and (*b*) for $x = 0.5$ and 0.7. Inset in (*b*) shows the data for La_2TiNiO_6

low temperature transitions as well as low temperature magnetic frustration merged together. For complete substitution of Mn by Ti i.e. $x = 1.0$ sample does not show any anomaly in the magnetization data and ZFC-FC superimposed as shown in inset of Fig. 2, *b*. This behaviour is typical for a paramagnetic material. This suggests that La_2TiNiO_6 does not show any kind of long-range ordering.

The gradual change in magnetic properties with replacement of magnetic Mn^{4+} by nonmagnetic Ti^{4+} in La_2MnNiO_6 is also supported from the isothermal magnetization data measured at 5 K under an applied field of ±5 T (Fig. 3). There is also a systematic decrease in magnetization as expected for magnetic dilution, but all the samples up to $x = 0.7$ exhibit clear hysteresis loop suggesting the prevalence of ferromagnetic component in the system. However, the opening of the loop is small as reported for the parent phase [15, 24]. There is no hysteresis loop for $x = 1.0$ sample (see inset in Fig. 3) which practically shows a linear increase in magnetization with field as expected for a paramagnet (see inset in Fig. 3).

Let us discuss the observed change in magnetization in $La_2Mn_{1-x}Ti_xNiO_6$. The substitution of Mn^{4+} by nonmagnetic Ti^{4+} will truncate the ferromagnetic $Ni^{2+} – O – Mn^{4+} – O – Ni^{2+}$ superexchange path to $Ni^{2+} – O – Ti^{4+} – O – Ni^{2+}$. This doping not only destroy the ferromagnetic exchange path, but also results in weak antiferromagnetic interaction between the Ni^{2+} cation. The weak antiferromagnetic interaction between Ni^{2+} takes place via super superexchage interaction mediated through $O – Ti^{4+} – O$ linker. This type of antiferromagnetic interaction is observed in half doped $LaNi_{0.5}Al_{0.5}O_3$ through Ni – O – Al – O – Ni exchange path [34]. Thus, with increase in Ti doping the ferromagnetism in La_2MnNiO_6 becomes more and more weaker as reflected by the change in T_C shown in Fig. 4. This result is very contrasting with the effect of Ti doping in single perovskite manganite $Sm_{0.55}Sr_{0.45}MnO_3$, where just 4% of Ti doping leads for disappearing of the ferromagnetic state [35]. The robustness of ferromagnetism towards magnetic dilution in double perovskite La_2MnNiO_6 may be related to the cationic ordering. Most likely the disruption of $Ni^{2+} – O – Mn^{4+} – O – Ni^{2+}$ superexchange path leads to fragmented

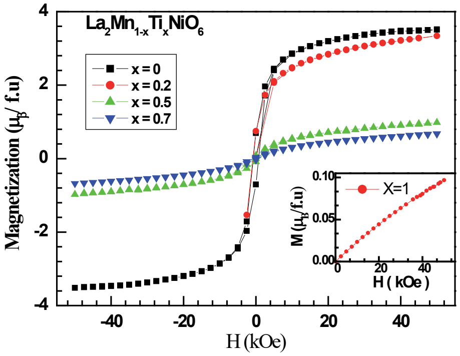

Fig. 3. Isothermal magnetization of $La_2Mn_{1-x}Ti_xNiO_6$ ($x = 0$, 0.2, 0.5 and 0.7) recorded at 5 K. Inset shows the data for La_2TiNiO_6

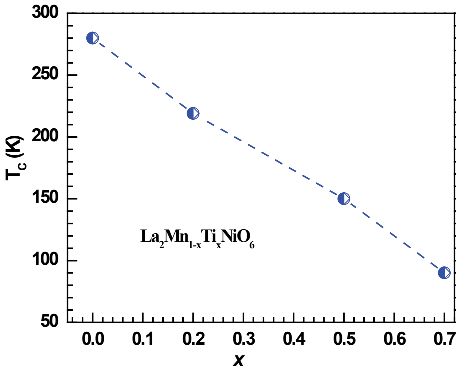

Fig. 4. Variation of ferromagnetic Curie temperature (T_C) with x in $La_2Mn_{1-x}Ti_xNiO_6$

ferromagnetic clusters which are responsible for observed magnetic behaviour of the Ti doped samples even for 70% doping. This is even higher than the effect of Ti doping in spinel structure. $Mn_{1+x}Fe_{2-2x}Ti_xO_4$ has been reported to exhibit ferrimagnetic ordering up to 50% Ti doping [36, 37]. However, one cannot rule out the cationic disordering with the increase in Ti doping. La_2CoTiO_6 and Pr_2CoTiO_6 have been reported to show long-range antiferromagnetism at 15 K and 17 K, respectively, in cationic ordered state. The antiferromagnetic exchange interaction path is $Co^{2+}-O-Ti^{4+}-O-Co^{2+}$ in cationic ordered samples [28, 29]. However, we did not observe any such long range antiferromagnetic ordering in La_2TiNiO_6. The absence of such long range ordering can be related to the cationic disordering.

To look at the magnetic features above T_C we have fitted the high temperature data with Curie-Weiss law. The calculated effective paramagnetic moments also found to decrease with the increase in Ti doping. The μ_{eff} value for the parent phase is 6.30 μ_B/f.u. which is slightly larger than the calculated value 5.97 μ_B/f.u., which has been attributed to the possible formation of ferromagnetic cluster above T_C [38, 39]. The μ_{eff} value decreases from 4.8 μ_B/f.u. for $x = 0.2$ to 1.72 μ_B/f.u. for $x = 1.0$ sample revealing the effect of magnetic dilution. Finally, to confirm the association of low temperature magnetic anomaly with spin glass behaviour as reported for the parent phase we have measured the ac-susceptibility of $x = 0$ and $x = 0.5$ samples at different driving frequencies in the low temperature regions. Fig. 5 shows the real and imaginary parts of the ac-susceptibility data for these two samples. The $\chi'(T)$ for $x = 0$ sample is too broad to uniquely identify the glass transition temperature T_g

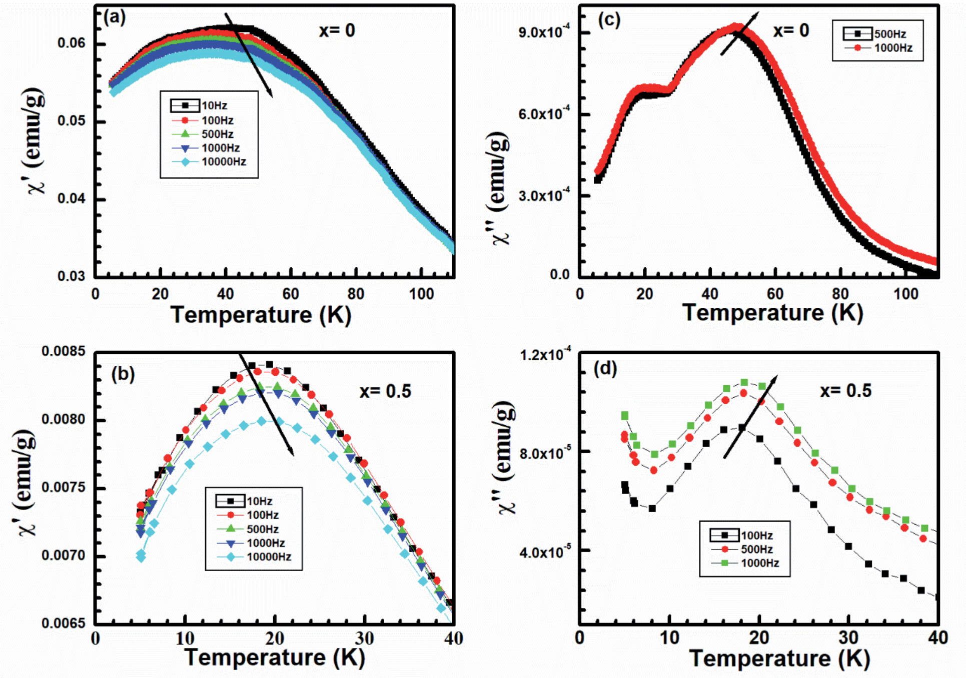

Fig. 5. Temperature dependent ac-susceptibilities of $La_2Mn_{1-x}Ti_xNiO_6$ for $x = 0$ and 0.5. Panels (*a, b*) show real part, $\chi'(T)$, and (*c, d*) show imaginary part, $\chi''(T)$, at selected frequencies

(Fig. 5, *a*). However, the χ”(*T*) revealed two frequency dependent peak around 20 K and 50 K (Fig. 5, *c*), respectively, suggesting the magnetic frustration. The multiglass behaviour of La_2MnNiO_6 has been reported in the literature [18]. This magnetic frustration is associated with the competing interaction between the antisite disorder induced antiferromagnetic $Mn^{4+}-O-Mn^{4+}$ and $Ni^{2+}-O-Ni^{2+}$ interactions and ferromagnetic clusters [18]. The $x = 0.5$ sample exhibit only one peak around 20 K, which is frequency dependent as revealed from both χ’(*T*) and χ”(*T*) data (Figs. 5, *b*, *d*). This indicates the presence of magnetic frustration in pure and Ti doped samples.

Conclusions

In the present study, we have synthesized $La_2Mn_{1-x}Ti_xNiO_6$ $(0 \leq x \leq 1.0)$ by modified citrate-based sol-gel method. Rietveld analysis of the PXRD patterns revealed that the parent phase ($x = 0$) is biphasic in nature composed of rhombohedral $R\overline{3}c$ and monoclinic $P2_1/n$ structures, whereas Ti doped samples crystalized in single phase monoclinic $P2_1/n$ structure with the suppression of rhombohedral phase. The cell volume of the Ti doped samples increased due to larger size of Ti^{4+} compared to Mn^{4+} ion. The magnetic measurements suggest the multiple magnetic transition in La_2MnNiO_6. The high temperature ferromagnetic transition with T_C~280 K associated with the cationic ordered ferromagnetic superexchange interaction $Ni^{2+}-O-Mn^{4+}$ becomes weaker by replacement of Mn^{4+} by nonmagnetic Ti^{4+}. There is a gradual shift in T_C with increase in Ti doping eventually leading to a paramagnetic state in La_2TiNiO_6. The ferromagnetic state of double perovskite exhibits robustness towards Ti substitution compared to the simple perovskite manganite as well as spinels, which may be related to the cationic ordering. Unlike other Ti containing double perovskite, La_2TiNiO_6 fails to show long-range antiferromagnetic ordering probably due to cationic disordering. Both the pure and Ti doped samples show magnetic frustration at lower temperatures.

Acknowledgements

The authors acknowledge the financial support from Indo-Russian project (INT/RUS/RFBR/P-239), Department of Science and Technology (DST), Government of India.

References

1. Raveau B, Seikh Md. M. Cobalt oxides: from crystal chemistry to physics, John Wiley & Sons; 2012.
2. Kobayashi KI, Kimura T, Sawada H, Terakura K, Tokura Y. Room-temperature magnetoresistance in an oxide material with an ordered double-perovskite structure, Nature. Nature. 1998; 395(6703):677–680.
   DOI: 10.1038/27167.
3. von Helmolt R, Wecker J, Holzapfel B, Schultz L, Samwer K. Giant negative magnetoresistance in perovskitelike $La_{2/3}Ba_{1/3}MnO_x$ ferromagnetic films. Phys. Rev. Lett. 1993; 71(14):2331–2333.
   DOI: 10.1103/PhysRevLett.71.2331.

4. Rao CNR, Raveau B. Colossal Magnetoresistance, Charge Ordering and Related Properties of Manganese Oxides,WORLD SCIENTIFIC; 1998.
5. Baettig P, Ederer C, Spaldin NA. First principles study of the multiferroics $BiFeO_3$,Bi_2FeCrO_6 and $BiCrO_6$: Structure, polarization and magnetic ordering temperature. Phys. Rev. B. 2005; 72(21):214105.
DOI: 10.1103/PhysRevB.72.214105.
6. Anderson M, Greenwood K, Taylor G, Poeppelmeier K. B-cation arrangements in double perovskites. Prog. Solid State Chem. 1993; 22(3):197–233.
DOI: 10.1016/0079–6786(93)90004-B.
7. Balcells L, Navarro J, Bibes M, Roig A, Martínez B, Fontcuberta J. Cationic ordering control of magnetization in Sr_2FeMoO_6 double perovskite. Appl. Phys. Lett. 2001; 78(6):781–783.
DOI: 10.1063/1.1346624.
8. Woodward PM. Octahedral Tilting in Perovskites. I. Geometrical Considerations Acta Crystallogr. Sect. B. Struct. Sci. 1997; 53(1):32–43.
DOI: 10.1107/S0108768196010713.
9. Bos J-WG, Attfield JP. Structural and Magnetic Properties of the Double Perovskite $LaCaMnNbO_6$. Z. Anorg. Allg. Chem. 2004; 630(13–14):2248–2252.
DOI: 10.1002/zaac.200400159.
10. Vasala S, Karppinen M. $A_2B'B''O_6$ perovskites: A review. Prog. Solid State Chem. 2015; 43(1–2):1–36.
DOI: 10.1016/j.progsolidstchem.2014.08.001.
11. Ortega N, Kumar A, Scott JF, Katiyar RS. Multifunctional magnetoelectric materials for device applications. J. Phys. Condens. Matter 2015; 27(50):504002.
DOI: 10.1088/0953–8984/27/50/504002.
12. Neenu Lekshmi P, Vasundhara M, Varma MR, Suresh KG, Valant M. Structural, magnetic and dielectric properties of rare earth based double perovskites RE_2NiMnO_6 (RE=La, pr, Sm, Tb). Phys. B Condens. Matter 2014; 448:285–289.
DOI: 10.1016/j.physb.2014.04.057.
13. Yadav R, Nair HS, Kumar A, Adiga S, Bhat HL, Yusuf SM, Elizabeth S. Investigation of dielectric relaxation, Jahn-Teller distortion, and magnetic ordering in Y substituted $Pr_{1-x}Y_xMnO_3(0.1 \leq x \leq 0.4)$. J. Appl. Phys. 2015; 117(9):093903.
DOI: 10.1063/1.4913881.
14. Rogado NS, Li J, Sleight AW, Subramanian MA. Magnetocapacitance and Magnetoresistance Near Room Temperature in a Ferromagnetic Semiconductor: La_2NiMnO_6. Adv. Mater. 2005; 17 (18):2225–2227.
DOI: 10.1002/adma.200500737.
15. Dass RI, Yan, J-Q, Goodenough JB. Oxygen stoichiometry, ferromagnetism, and transport properties of $La_{2-x}NiMnO_{6+\delta}$. Phys. Rev. B 2003; 68(6): 064415.
DOI: 10.1103/PhysRevB.68.064415.
16. Joly VLJ, Joy PA, Date SK, Gopinath CS. Two ferromagnetic phases with different spin states of Mn and Ni in $LaMn_{0.5}Ni_{0.5}O_3$. Phys. Rev. B 2002; 65(18): 184416.
DOI: 10.1103/PhysRevB.65.184416.

17. Biswal AK, Ray J, Babu PD, Siruguri V, Vishwakarma PN. Dielectric relaxations in La_2NiMnO_6 with signatures of Griffiths phase . J. Appl. Phys. 2014; 115(19):194106. DOI: 10.1063/1.4876723.
18. Choudhury D, Mandal P, Mathieu R, Hazarika A, Rajan S, Sundaresan A, Waghmare UV, Knut R, Karis O, Nordblad P, Sarma DD. Near-Room-Temperature Colossal Magnetodielectricity and Multiglass Properties in Partially Disordered La_2MnNiO_6. Phys. Rev. Lett. 127201. doi:10.1103/PhysRevLett.108.127201. 2012;108(12):127201.
19. Mondal P, Bhattacharya D, Choudhury P, Mandal P. Dielectric anomaly at T_N in $LaMnO_3$ as a signature of coupling between spin and orbital degrees of freedom. Phys. Rev. B 2007; 76(17):172403.
DOI: 10.1103/PhysRevB.76.172403.
20. Ricciardo RA, Hauser AJ, Yang FY, Kim H, Lu W, Woodward PM. Structural, magnetic, and electronic characterization of double perovskites $BixLa_{2-x}MnMO_6$ (M = Ni, Co; x = 0.25, 0.50). Mater. Res. Bull. 2009; 44(2):239–247.
DOI: 10.1016/j.materresbull.2008.10.015.
21. Sayed FN, Achary SN, Jayakumar OD, Deshpande SK, Krishna PSR, Chatterjee S, Ayyub P, Tyagi AK. Role of annealing conditions on the ferromagnetic and dielectric properties of La_2NiMnO_6. J. Mater. Res. 2011; 26(4):567–577.
DOI: 10.1557/jmr.2011.4.
22. Gaikwad VM, Yadav KK, Lofland SE, Ramanujachary KV, Chakraverty S, Ganguli AK, Jha M. New low temperature process for stabilization of nanostructured La_2NiMnO_6 and their magnetic properties. J. Magn. Magn. Mater. 2019; 471:8–13.
DOI: 10.1016/j.jmmm.2018.08.081.
23. Biswal AK, Ray J, Babu PD, Siruguri V, Vishwakarma PN. Effect of Cu substitution on the magnetic and dielectric properties of La_2NiMnO_6. J. Appl. Phys. 2015; 117(17):17B728.
DOI: 10.1063/1.4917069.
24. Yuan X, Li Q, Hu J, Xu M. Unusual dynamic magnetic behavior of polycrystalline La_2NiMnO_6. Phys. B Condens. Matter 2013; 424:73–78.
DOI: 10.1016/j.physb.2013.04.057.
25. Chandrasekhar KD, Das AK, Venimadhav A. Spin glass behaviour and extrinsic origin of magnetodielectric effect in non-multiferroic La_2NiMnO_6 nanoparticles. J. Phys. Condens. Matter 2012; 24(37):376003.
DOI: 10.1088/0953–8984/24/37/376003.
26. Dass RI, Goodenough JB. Multiple magnetic phases of $La_2CoMn_{6-\delta}$ ($0<\sim\delta<\sim0.05$). Phys. Rev. B 2003; 67(1):014401.
DOI: 10.1103/PhysRevB.67.01440.
27. Blasse G. Magnetic properties of mixed metal oxides with ordered perovskite structure. Philips Res. Rep. 1965; 20:327.
28. Holman KL, Huang Q, Klimczuk T, Trzebiatowski K, Bos JWG, Morosan E, Lynn JW, Cava RJ. Synthesis and properties of the double perovskites La_2NiVO_6, La_2CoVO_6, and La_2CoTiO_6. J. Solid State Chem. 2007; 180(1):75–83.
DOI: 10.1016/j.jssc.2006.09.013.

29. Das N, Singh R, Das A, Gupta LC, Ganguli AK. Structural, magnetic and dielectric properties of a new double perovskite Pr_2CoTiO_6. J. Solid State Chem. 2017; 253:355–359.
    DOI: 10.1016/j.jssc.2017.06.024.
30. Shannon RD. Revised effective ionic radii and systematic studies of interatomic distances in halides and chalcogenides. Acta Crystallogr. Sect. A 1976; 32(5):751–767.
    DOI: 10.1107/S0567739476001551.
31. Rodríguez-Carvajal. Recent advances in magnetic structure determination by neutron powder diffraction J. Phys. B Condens. Matter 1993; 192(1–2):55–69.
    DOI: 10.1016/0921–4526(93)90108-I.
32. Blasco J, Sánchez MC, Pérez-Cacho J, García J, Subías G, Campo J. Synthesis and structural study of $LaNi_{1-x}Mn_xO_{3+\delta}$ perovskites J. Phys. Chem. Solids 2002; 63(5):781–792.
    DOI: 10.1016/S0022-3697(01)00228–1.
33. Azuma M, Takata K, Saito T, Ishiwata S, Shimakawa Y, Takano M. Designed Ferromagnetic, Ferroelectric Bi_2NiMnO_6. J. Am. Chem. Soc. 2005; 127(24):8889–8892.
    DOI: 10.1021/ja0512576.
34. Palakkal JP, Sankar CR, Varma MR. Magnetism and magnetoresistance in Al half doped $LaNiO_3$. Mater. Chem. Phys. 2019; 225:316–319.
    DOI: 10.1016/j.matchemphys.2019.01.001
35. Sarkar P, Khan N, Pradhan K, Mandal P. Collapse of ferromagnetism with Ti doping in $Sm_{0.55}Sr_{0.45}MnO_3$. Phys. Rev. B 2018; 98(1): 014422.
    DOI: 10.1103/PhysRevB.98.014422
36. Mujasambatoo K, Kumar S, Ansari MS. Ferrimagnetic Ordering of Ti^{4+} Doped $Mn_{1+x}Fe_{2-2x}O_4$ $(0 \le x \le 0.5)$ Ferrites at Room Temperature. Sci. Adv. Mater. 2011; 3(1):120–126.
    DOI: 10.1166/sam.2011.1143
37. Kumar S, Koo BH, Lee CG, Gautam S, Chae KH. Magnetic and Electronic Structure Studies of $Mn_{1+x}Fe_{2-2x}Ti_xO_4$ $(0 \le x \le 0.5)$ Ferrites. Funct. Mater. Lett. 2010; 03(04):269–273.
    DOI: 10.1142/S1793604710001391.
38. Devi Chandrasekhar K, Das AK, Mitra C, Venimadhav A. The extrinsic origin of the magnetodielectric effect in the double perovskite La_2NiMnO_6. J. Phys. Condens. Matter 2012; 24(49):495901.
    DOI: 10.1088/0953–8984/24/49/495901.
39. Zhou S, Shi L, Yang H, Zhao J. Evidence of short-range magnetic ordering above T_C in the double perovskite La_2NiMnO_6. Appl. Phys. Lett. 2007; 91(17):172505.
    DOI: 10.1063/1.2801694

Beketov I. V., Safronov A. P., Medvedev A. I.,
Murzakaev A. M., Zhidkov I. S., Cholah S. O., Maximov A. D.
Chimica Techno Acta. 2019. Vol. 6, No. 3. P. 93–103.
ISSN 2409–5613

DOI: 10.15826/chimtech.2019.6.3.02

I. V. Beketov[a*], **A. P. Safronov**[a,b], **A. I. Medvedev**[a,b],
A. M. Murzakaev[a,b], **I. S. Zhidkov**[b],
S. O. Cholah[b], **A. D. Maximov**[a]
[a] Institute of Electrophysics UB RAS,
106 Amundsen St., Yekaterinburg, 620016, Russian Federation
[b] Ural Federal University,
19 Mira St., Yekaterinburg, 620002, Russian Federation
**E-mail: beketov@iep.uran.ru*

Encapsulation of Ni nanoparticles with oxide shell in vapor condensation

Controlled input of oxygen into the inert working gas flow during the production of Ni nanoparticles by the electrical explosion of wire (EEW) method leads to the formation of a crystalline oxide shell on the surface of particles during their condensation from the vapor phase. Resulting oxide shells encapsulating Ni particles weaken their agglomeration processes as well as protect the surface of the Ni nanoparticles from further oxidation. The influence of the amount of energy introduced during EEW and the quantity of oxygen added to the working gas in EEW process on the properties of resulting Ni nanoparticles was studied. The obtained nickel nanopowders were characterized by X-ray diffraction (XRD), transmission electron microscopy (TEM), X-ray photoelectron spectroscopy (XPS), and N_2 adsorption (BET) methods, which gave the specific surface area, the average diameter of nanoparticles, their phase composition, the morphology of the particles and the structure of the oxide shells. It was shown that the addition of oxygen leads to a decrease in the average diameter of Ni nanoparticles and reduces the degree of their agglomeration. The encapsulation of Ni nanoparticles with 3–5 nm thick gas-tight oxide shells protects the particles from oxidation and eliminates the pyrophoricity of the powder product.

Keywords: nickel nanoparticles, oxide shells, encapsulation, electrical explosion of wire.

Received: 10.07.2019. Accepted: 16.09.2019. Published: 15.10.2019.

Introduction

Today, nanoparticles of transition metals are of considerable interest both from a scientific point of view due to their specific physical and chemical properties, and also in connection with promising practical applications [1]. In particular, such materials can be used as catalysts, as components in magnetic recording systems, in bioengineering and biomedicine, as components in sensors, actuators, scaffolds, etc.

With a decrease in particle size their surface activity considerably increases, promoting agglomeration and aggregation of particles, which complicates their further use. For instance, in the preparation of metal matrix composites or complex ceramic composites, the uniformity of the material is achieved only at the scale of agglomerates with sizes varying from units to tens of micrometers. Thus, the agglomeration of nanoparticles during their production limits the yield: with a decrease in the size of the particles, it is necessary to reduce the productivity of equipment to prevent their agglomeration. In addition, it is known that metal nanoparticles, with the exception of noble metals, are very pyrophoric at low temperatures and simply combust if exposed to ambient air. Usually, after the synthesis, the metal nanoparticles are passivated: a thin layer of oxide, which subsequently protects the metal from rapid oxidation, is formed on their surface. However, some metals, such as Cu, even after the passivation do not form a gas-tight oxide shell that protects them from further oxidation. In particular, it is shown [2] that the process of oxidation of copper nanoparticles during their storage in air results in complete formation of CuO.

To prevent agglomeration and to protect the surface of the particles, it is desirable to form protective shells on the particles during their formation. A choice of a material for a protective cover is a separate issue. On the one hand, the most acceptable material for the protective shell is a material that reliably protects the surface of the particle from rapid oxidation and does not interfere with, and in some cases even contributes to the further use of such powders. On the other hand, nanoparticles with the structure of the metal core — protective shell are typically used as fillers in composite polymer materials and liquid disperse systems. Therefore, the main property of the shell material is also to ensure the compatibility of core/shell nanoparticles with the dispersion medium, which depends on the energy of interaction between the dispersion medium and the surface of such nanoparticles.

In the technology of synthesis of metal nanoparticles, their surface is typically covered with pure carbon, silicon carbide, or polyethylene [3], which are not active at low temperatures. For instance, to create a carbon protective shell on the particles, various methods are used, such as annealing of metal particles in the atmosphere of hydrocarbon (gasoline) [4], filling carbon tubes with metal [5], annealing of a mixture of metal powder with carbon [6]. All these techniques involve the processing of the finished powder. The formation of a carbon shell on the surface of the particles in the process of synthesis of Fe, Co, Ni metal nanoparticles and their alloys using the method of an arc discharge in the methane atmosphere is described in Ref. [7].

In our opinion, nickel monoxide (NiO) is a promising material of the protective shell for Ni nanoparticles. NiO has a relatively high melting point, 1955 °C [8], and it forms a strong gas-tight protective film on the metal surface [9]. The objective of the present study is to develop an in-situ method of the formation of the protective oxide shells on the surface of Ni nanoparticles during their synthesis by the electric explosion of wire. Electric explosion of wire (EEW) is one of the most productive methods of synthesis of nanoparticles of metals, alloys and their chemical compounds. The productivity of EEW method ranges from 50 to 500 g/h depending on the nature of nanoparticles. The method has low energy consumption, not exceeding 50 kW·h/kg; it is environmentally friendly; it provides high purity of the resulting particles. Experimental setups for EEW method are compact and do not require separate facilities. This method has been described in detail elsewhere [10].

Experimental

Production of nickel nanopowders was carried out in the installation of an electric explosion of wire (EEW). The discharge circuit had an inductance of 0.4 μH. The capacitance of the capacitor bank varied from 3.2 to 4.8 μF, and the charging voltage — from 20 to 30 kV, which provided a change in overheating ratio *k* (the ratio of the energy introduced into the wire to the sublimation energy of the wire metal) in the range of 1–2.2. To obtain the powder, a wire of nickel (NP2 grade) with a diameter of 0.3 mm and a length of 88 mm was used. The wire was fed into an explosion chamber continuously. Wire explosions were carried out in argon at a pressure of 0.12 MPa at a frequency of 0.5 Hz.

The gas system of the installation consisted of an explosion chamber, two inertial traps with a gas flow rotation, a mechanical (cloth) filter and a fan connected in series. Inertial traps were used to separate large micron-sized particles; the rest of the powder was collected in the filter. As shown by preliminary experiments, the output of the powder in the filter depends on the amount of energy introduced into the wire and averages 85% of the mass of all resulting from the explosion powder. Only the powders from the filter were studied in the present work. To create shells on the surface of the particles in the process of the powder production, oxygen was continuously introduced into the working gas (Ar) flow directly before entering the explosion chamber. With the help of an adjustable flow-type throttle, the oxygen flow could vary from 0.3 to 20 cm^3/s. For the ease of comparison of powders obtained in different modes, the amount of oxygen is given below in grams per gram of nickel (g/g Ni). At low oxygen consumption, after producing the powder, it was additionally passivated with oxygen flow (0.5 cm^3/s) supplied to the EEW setup. The minimum oxygen consumption, which allows eliminating the pyrophoricity of the powder, was determined experimentally. The passivation process was controlled by the oxygen partial pressure sensor. Passivation stopped when the partial pressure of oxygen reached 2 kPa. After that, the powder was freely (without the risk of its self-combustion) removed to the air.

The specific surface area of the obtained powders was determined by the BET method by low-temperature nitrogen adsorption using Micromeritics TriStar 3000. X-ray phase analysis (XRD) was performed on the Bruker D8 DISCOVER diffractometer in Cu Kα radiation (λ = 1.54 Å) with a graphite monochromator on the secondary beam. Processing of diffractograms was performed using the program TOPAS 3. High-resolution transmission electron microscopy (TEM) was performed using the JEOL JEM2100 electron microscope at an accelerating voltage of 200 kV. The energy introduced into the wire was determined by the oscillograms of the current pulse passing through the exploding section of the wire. Measurements of the X-ray photoelectron spectroscopy (XPS) spectra of the main and valence levels of powders were carried out on the spectrometer PHI 5000 VersaProbe, based on the classical scheme of X-rays with a quartz monochromator and a hemispherical energy analyzer operating in the energy range from 0 to 1500 eV. Electrostatic focusing with magnetic shielding allows obtaining energy resolution Δ$E \leq 0.5$ eV for Al Kα radiation (1486.6 eV). Pumping of the analytical chamber was carried out with the help of an ion pump, which provides a pressure lower than 10^{-7} Pa. Two-channel neutralization was used to compensate the local surface charge formed during the measurements. The diameter of the X-ray spot was 200 mcm and X-ray power — 50 W. Calibration of spectra was carried out at the position of the 1s line of carbon $E = 285.0$ eV. Processing of XPS experimental data was carried out using the complex ULVAC-PHI MultiPak Software 9.8.

Results and discussion

The major variable to control the size of metal particles in EEW method is the overheating ratio (*k*). It is a dimensionless coefficient, which is equal to the electrical energy introduced into a portion of a metal wire subjected to EEW divided by the energy of sublimation of this metal. In case of Ni, the energy of sublimation is 65.1 J/mm^3. The experimental dependence of the specific surface area and the mean diameter of Ni nanoparticles on overheating coefficient are shown in Fig. 1. The mean diameter of spherical particles (*D*) is related to the value of their specific surface area (S_{sp}) by the following equation:

$$D = 6/\rho \cdot S_{sp}, \qquad (1)$$

with ρ being the effective density of the material (Ni — 8.91 g/cm^3, NiO — 7.45 g/cm^3).

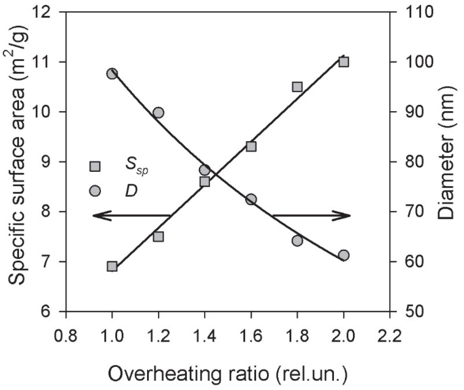

Fig. 1. The dependence of the specific surface area (left) and the average diameter (right) of Ni nanoparticles synthesized by EEW method on the overheating ratio

It is seen that the specific surface area of Ni nanoparticles substantially increases from around 7 m^2/g up to 11 m^2/g if the overheating ratio is doubled. Consequently, with the increase in the overheating ratio, the diameter of Ni particles diminishes from 100 down to 60 nm in average. Further on, the results for two values of the overheating ratio will be systematically compared. These values are $k = 1.2$, which corresponds to large Ni particles (low specific surface area) and $k = 2$ (small particles, high specific surface area). It is worth noting that overheating ratio $k = 1$ was not taken, because of the technical difficulties of maintaining stable EEW process at zero overheating.

Using the given levels of overheating ratio, several batches of Ni particles were synthesized with the controlled addition of oxygen to the EEW installation. The crystalline structure of obtained Ni nanoparticles was characterized by XRD. Fig. 2, *a* gives examples of XRD diffractograms for two Ni batches synthesized at different amount of oxygen added to the working gas of the EEW installation. In both cases, two cubic phases were identified: the major one corresponded to Ni with lattice parameter $a = 3.523(1)$ Å and the minor one corresponded to NiO with $a = 4.174(2)$ Å. It means that the addition of oxygen to the working gas resulted in the in-situ oxidation of condensed Ni nanoparticles. Further on, the obtained particles, which contain both the fraction of metallic Ni and NiO are denoted as Ni@NiO.

Using the diffractograms, the weight fraction of NiO in all batches was evaluated. The dependence of NiO content in nanoparticles on the amount of oxygen added to the working gas in EEW installation is given in Fig. 2, *b*. The amount of oxygen (in weight) is divided by the weight of Ni wire consumed in the synthesis. Further on it is denoted as *Q*. Experimental points in Fig. 2, *b* relate to two values of overheating ratio, $k = 1.2$ and $k = 2$.

It is seen that, despite the difference in the level of overheating ratio, the experimental points can be fitted well with the same linear dependence, %NiO = $302 \cdot Q$. It means that in-situ oxidation does not depend on the average diameter of Ni particles and is governed exclusively by the amount of oxygen in the working gas.

Fig. 3 presents experimental dependences of the specific surface area (Fig. 3, a)

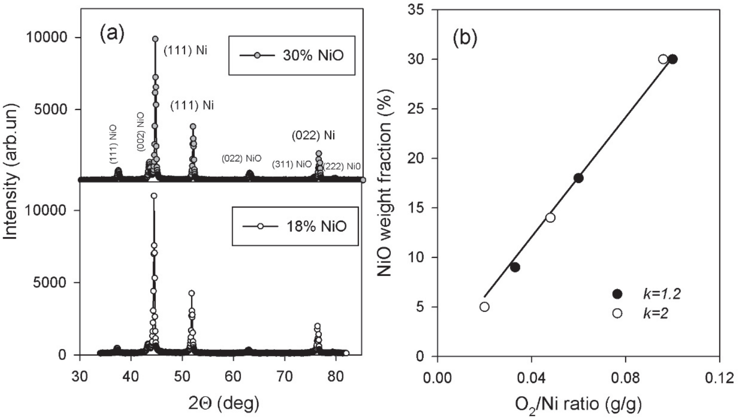

Fig. 2. *a* — Selected XRD diffraction patterns of EEW Ni nanoparticles synthesized with the addition of oxygen; *b* — Dependence of NiO weight fraction on the amount of oxygen added to EEW synthesis per Ni wire consumption. Closed circles correspond to overheating ratio 1.2, open circles — to overheating ratio 2

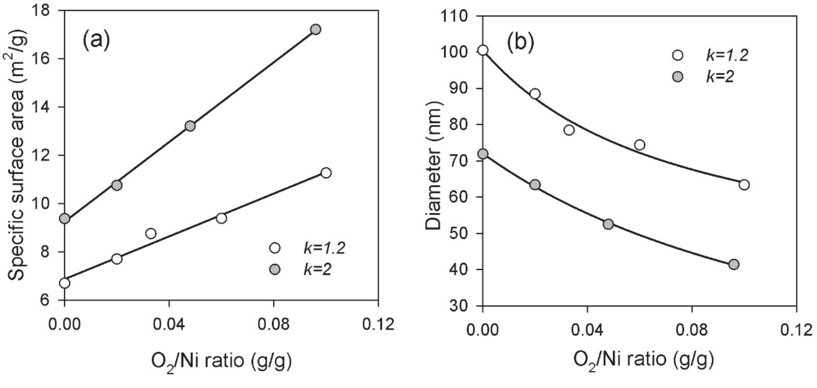

Fig. 3. Dependence of the specific surface area (*a*) and mean diameter (*b*) of Ni particles on the amount of oxygen introduced into EEW installation during the synthesis at overheating ratios 1.2 and 2

and the average diameter of nanoparticles (Fig. 3, *b*) on the amount of oxygen added to the working gas of the EEW installation at the values of overheating ratio equal to 1.2 and 2.

As shown in Fig. 3, *a*, the increase in oxygen consumption leads to an increase in the specific surface area of produced Ni nanoparticles at both levels of overheating ratio. The experimental plots are nicely fitted by the linear dependences: $6.9+44.2\cdot Q$ ($R^2 = 0.981$) for $k = 1.2$ and $9.2+82.4\cdot Q$ ($R^2 = 0.998$) for $k = 2$. In general, the increasing trend in specific surface area due to the addition of oxygen is equivalent to the same trend due to the increase in overheating ratio (see Fig. 1). It is because the oxidation of Ni to Ni oxide is accompanied with the evolution of heat, which adds up to the electric energy introduced in EEW. Thus, the total amount of energy (electrical and oxidation) in EEW process exceeds the sublimation energy of Ni significantly more in the presence of oxygen than in the inert atmosphere.

Fig. 3, *b* presents the average diameter of Ni@NiO particles as a function of oxygen/Ni ratio. The average diameter was calculated using Eq. (1) taking into account that the density of Ni@NiO particles diminishes with the increase of NiO content due to the difference in densities of Ni and NiO. It is seen that, at both levels of overheating ratio, the decreasing trend in the average diameter of Ni@NiO particles is observed. The reason is the same as for the increasing trend of the specific surface area. The oxidation reaction provides extra energy to the system, and the overheating effectively increases.

It is noticeable that the slopes of the linear plots in Fig. 3, *a* are different for two levels of overheating. The slope coefficient is 44.2 if $k = 1.2$, and it is 82.4 if $k = 2$. However, no evident difference in the slopes of plots can be noticed in Fig. 3, *b*. It is because the calculation of the average diameter of Ni@NiO particles according to Eq. (1) includes the partial correction of increasing S_{sp} values by the decreasing density of Ni@NiO particles with the increase in their oxidation. The plots are shifted one against the other by the initial difference of average particle diameter for $k = 1.2$ (smaller particles) and $k = 2$ (larger particles).

It is known [9] that in the oxidizing atmosphere the surface of metallic Ni is covered with dense oxide layer which efficiently prevents metal from further oxidation. The Pilling-Batworth criterium [11] for NiO is 1.52, which means that Ni particles should be covered with dense oxide shell in the presence of oxygen. During EEW, the formation of oxide shells on the surface of Ni particles can start only at the moment when the expanding cloud of metal vapor after the explosion mixes up with the working gas, which contains oxygen. It does not take place at the very first moments after the explosion, as the expanding cloud of vapors is substantially denser than the surrounding working gas. Furthermore, the critical temperature of the thermodynamic stability of NiO is lower than the temperature of condensation of Ni vapors into liquid phase. Therefore, oxidation begins when the condensation on Ni liquid droplets has been already completed, and it takes place at the surface of Ni particles (liquid or solid). Fig. 4 presents high-resolution TEM image of the surface of Ni particle synthesized in the presence of oxygen.

It is clearly noticeable that the surface of a particle is covered with a layer, whose crystal structure is different from that of the interior of the particle. The lattice period in the surface layer evaluated from HRTEM images is 2.4±0.1 Å. This value corresponds to the lattice period for cubic or rhombohedric NiO structure. According to XPS analysis, the spectrum of the surface of Ni particles synthesized in the presence of oxygen contained signals of elements Ni and O. Ni is present in the oxidation state Ni^{+2}, which is an indication of NiO [12], and Ni^{+3}, which likely corresponds to Ni_2O_3 [13] or NiOOH [14]. The surface also contained carbon, which is the result of carbon dioxide adsorption from the air.

The thickness of oxide layers on Ni particles was evaluated by the graphical analysis of TEM images obtained with $3.7 \cdot 10^6$ and $7.4 \cdot 10^6$ magnification. The average values of the thickness of oxide layers are given in Table 1. According to Table 1, the thickness of oxide layers increases with the increase in the amount of oxygen added to working gas in EEW process. At the same time, the overheating ratio does not make a noticeable influence.

Table 1

Average thickness of oxide layer on Ni@NiO particles

Q_{O2}, g/g Ni	Overheating, *k*	Thickness, nm
0.03	1.2	2.51
0.1	1.2	3.35
0.02	2	2.82
0.096	2	3.31

Like other chemical reactions in the EEW process, oxidation of Ni surface takes place in non-equilibrium conditions. It results in the non-uniformity of NiO distribution on the surface of Ni@NiO particles. It becomes more evident at large amounts of added oxygen. Fig. 5 presents TEM image of Ni@NiO particles obtained at $Q_{O_2} = 0.1$ g/g Ni.

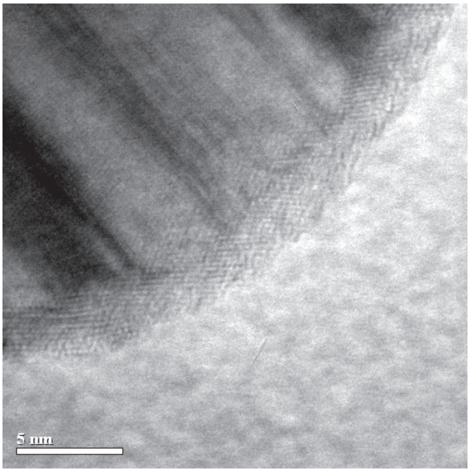

Fig. 4. High-resolution TEM image of Ni particle synthesized by EEW at $k = 1.2$; $Q_{O2} = 0.033$ g/g Ni

It is noticeable in Fig. 5, *a* that the spherical shape of Ni@NiO particles became substantially distorted due to the formation of oxide layers with varied thickness. Most likely, it is because oxidation took place at elevated temperature before the particles were cooled down to the ambient temperature. In these conditions of intense non-equilibrium oxidation, the initially formed oxide layer could be fractioned, and spherical shape of particles would be distorted. Such distortions might as well be taken as evidence in favor of oxidation of Ni in liquid droplets, whose surface is easier to distort, rather than condensed solid particles.

At the high level of oxygen in the working gas, the smallest Ni particles, which are the most chemically active, could transform completely into NiO. Fig. 5, *b* shows such a particle with a diameter of 15 nm, which is completely formed by NiO. The fragment of crystal lattice noticeable in Fig. 5, *b* has a lattice period of 2.4±0.1 Å, which corresponds to NiO. Due to the presence of separate NiO particles and thickened oxide layers, the total NiO content in Ni@

NiO particles according to XRD increases up to 30% if oxygen content in the working gas is raised up to 0.1 g/g Ni.

As the oxidation of Ni likely takes place on the surface of liquid droplets, the formation of solid oxide layer can prevent the coalescence of droplets, which causes agglomeration of particles in the product powder. Fig. 6 illustrates the influence of oxygen addition on agglomeration.

In Fig. 6, *a* it is evident that agglomeration of Ni particles is high. Almost all of them in the image are bonded into one cluster, which is certainly the result of coalescence of liquid Ni droplets in gas phase at temperatures above crystallization. Con-

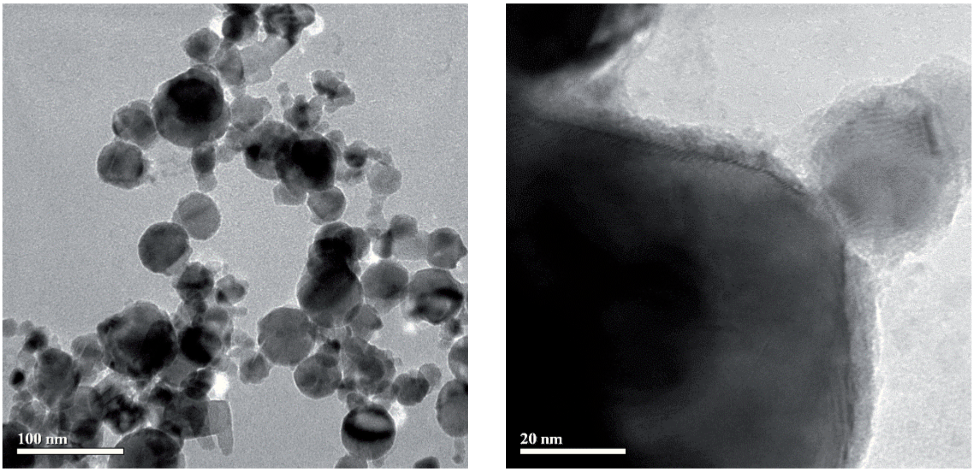

a *b*

Fig. 5. *a* — Ni@NiO particles obtained by EEW at $Q_{O2} = 0.1$ g/g Ni, $k = 1.2$; *b* — High resolution TEM image of the surface with NiO layer and small separate NiO particle (D = 15 nm)

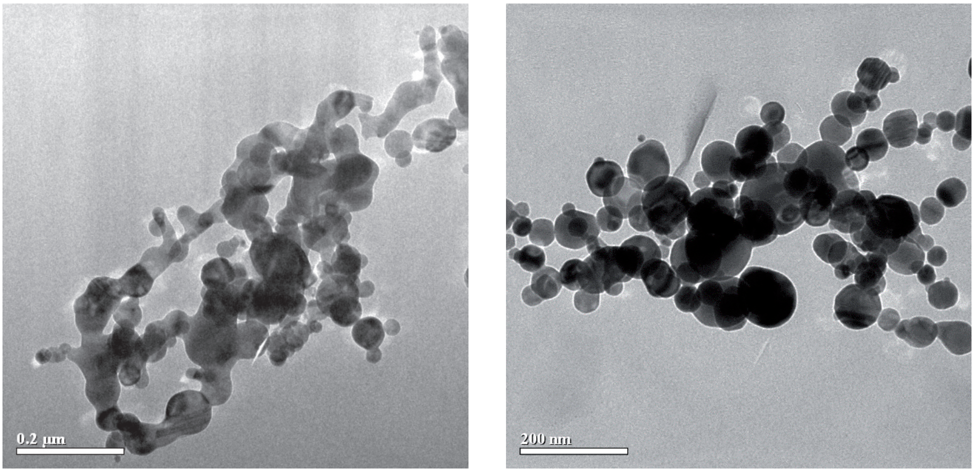

a *b*

Fig. 6. *a* — Ni nanoparticles synthesized in argon; *b* — Ni@NiO nanoparticles synthesized in argon with the addition of oxygen, $Q_{O2} = 0.033$ g/g Ni

trary to that, the majority of Ni@NiO nanoparticles in Fig. 6, *b* are separated from each other. Even if we see them on top of one another, we can also see distinct spherical boundaries. It means that Ni@NiO particles are individual. Some agglomeration can still be noticed, but it is not predominant in case of Ni@NiO particles. The residual agglomeration of Ni@NiO stems from the large difference — 1223 K — between the temperature of vaporization of Ni, 3173 K [15], and the upper temperature of oxidation, 1950 K (calculated using the software Chemical WorkBench, ver. 3, Kinetic Technologies Ltd.). This temperature interval provides a time gap from the moment when liquid droplets of Ni condense from the vapor phase until they are covered with solid oxide, which prevents their coalescence. In case of other metals, this interval is narrower: Al — 350–400 K, Cu — 500 K. In case of these metals, the addition of oxygen prevents agglomeration completely. Nevertheless, despite the large temperature interval before oxidation, the addition of oxygen substantially decreases agglomeration of Ni nanoparticles.

NiO layers on the surface of Ni nanoparticles substantially enhance their stability to self-combusting in the air. It was found experimentally that at an oxygen consumption greater than 0.015 g/g Ni, the powdered product can be transferred from the EEW setup to the ambient air without the risk of combustion. Such oxygen addition leads to a significant reduction in the pyrophoricity of the powder, as Ni@NiO particles are covered with an oxide shell that reliably protects them from oxidation during storage.

Conclusions

The controlled oxygen injection into the inert working gas of the EEW unit during the production of Ni powder makes it possible to form a crystalline oxide shell on the particles in the process of their formation. It depresses the particle agglomeration, as well as protects the surface of Ni particles from oxidation. The increase in oxygen consumption leads to an increase in the specific surface area of the powder. In the range of oxygen consumption from 0 to 0.1 g/g Ni, the specific surface area varies almost linearly and increases by 60–80% depending on the overheating ratio.

Addition of oxygen to the working gas leads to the formation of a separate phase in the powdered product — crystalline Ni oxide, the content of which increases with increasing oxygen consumption. At low consumption of oxygen, NiO forms a dense crystalline shell on the surface of particles. The thickness of the shell is 2–5 nm and increases with increasing oxygen consumption. Overheating ratio has no significant effect on the shell thickness. In the range of oxygen consumption 0–0.1 g/g Ni the content of NiO linearly increases up to 30% independently of overheating ratio. At high oxygen consumption, spherical shape of Ni@NiO nanoparticles is substantially distorted, and small separate individual NiO nanoparticles tend to appear. When the oxygen consumption is larger than 0.015 g/g Ni, the powdered product becomes non-pyrophoric and can be subjected to the ambient air without the risk of combustion.

Acknowledgements

This work was performed as part of State Task of IEP UB RAS and by RAS Program Project No. 18-10-2-38. The study was performed using the equipment of the Center for the common research of IEP UB RAS and using the X-ray spectrometer of the Chair of Electrophysics of the Physical Technological Institute of the Ural Federal University.

References

1. Gusev AI. Nanomaterialy, nanostructury, nanotekhnologii. Moscow: Fizmatlit, 2005. 416 p. Russian.
2. Kotov YuA, Rhee ChK, Beketov IV, Bagazeyev AV, Demina TM, Murzakayev AM, Samatov OM, Timoshenkova OR, Medvedev AI, Shtols AK. Production of Copper Nanopowders by Electric Explosion of Wire-Study of Their Oxidation during Storage and Heating in Air. Journal of Metastable and Nanocrystalline Materials. 2003;15–16:343–8.
   DOI: 10.4028/www.scientific.net/JMNM.15–16.343.
3. Athanassiou EK, Grass RN, Stark WJ. Large-scale production of carbon-coated copper nanoparticles for sensor applications. Nanotechnology. 2006;17(6):1668–73.
   DOI: 10.1088/0957–4484/17/6/022.
4. Hayashi C. Ultrafine particles. Journal of Vacuum Science & Technology A. 1987;5(4):1375–84.
   DOI: 10.1116/1.574773.
5. Tsang SC, Chen YK, Harris PJF, Green MLH. A simple chemical method of opening and filling carbon nanotubes. Nature. 1994;372(6502):159–62.
   DOI: 10.1038/372159a0.
6. Tomita S, Hikita M, Fujii M, Hayashi S, Akamatsu K, Deki S, Yasuda H. Formation of Co filled carbon nanocapsules by metal-template graphitization of diamond nanoparticles. Journal of Applied Physics. 2000;88(9):5452–6.
   DOI: 10.1063/1.1317242.
7. Zhang ZD, Zheng JG, Skorvanek I, Wen GH, Kovac J, Wang FW, Yu JL, Li ZJ, Dong XL, Jin SR, Liu W, Zhang XX. Shell/core structure and magnetic properties of carbon-coated Fe-Co(C) nanocapsules. Journal of Physics: Condensed Matter. 2001;13(9):1921–9.
   DOI: 10.1088/0953–8984/13/9/314.
8. Wartenberg HV, Reusch HJ, Saran E. Schmelzpunktsdiagramme höchstfeuerfester Oxyde. VII. Systeme mit CaO und BeO. Zeitschrift für anorganische und allgemeine Chemie. 1937;230(3):257–76. German.
   DOI: 10.1002/zaac.19372300309.
9. Evans UR. Corrosion and Oxidation of Metals. London: Edward Arnold Ltd., 1960. 324 p.
10. Kotov YA. Electric Explosion of Wires as a Method for Preparation of Nanopowders. Journal of Nanoparticle Research. 2003;5(5):539–50.
    DOI: 10.1023/B:NANO.0000006069.45073.0b.
11. Pohil PF, Belyaev AF et al. Gorenie poroshkoobraznykh metallov v aktyivnykh sredakh. Moscow: Nauka, 1972. 294 p. Russian.

12. Payne BP, Biesinger MC, McIntyre NS. The study of polycrystalline nickel metal oxidation by water vapour. Journal of Electron Spectroscopy and Related Phenomena. 2009;175(1):55–65.
DOI: 10.1016/j.elspec.2009.07.006.
13. Weidler N, Schuch J, Knaus F, Stenner P, Hoch S, Maljusch A, Schäfer R, Kaiser B, Jaegermann W. X-ray Photoelectron Spectroscopic Investigation of Plasma-Enhanced Chemical Vapor Deposited NiO_x, $NiO_x(OH)_y$, and $CoNiO_x(OH)_y$: Influence of the Chemical Composition on the Catalytic Activity for the Oxygen Evolution Reaction. Journal of Physical Chemistry C. 2017;121(12):6455–63.
DOI: 10.1021/acs.jpcc.6b12652.
14. Leedahl B, Boukhvalov DW, Kurmaev EZ, Kukharenko A, Zhidkov IS, Gavrilov NV, Cholakh SO, Huu Le P, Wei Luo C, Moewes A. Bulk vs. Surface Structure of 3d Metal Impurities in Topological Insulator Bi_2Te_3. Scientific Reports. 2017;7(1):5758.
DOI: 10.1038/s41598-017-06069-3.
15. Perel'man FM, Zvorykin AYa. Kobalt i nikel. Moscow: Nauka, 1975. 215 p. Russian.

Redkin A. A., Pershina S. V., Il'ina E. A., Kataev A. A., Zaikov Yu. P.
Chimica Techno Acta. 2019. Vol. 6, No. 3. P. 104–110.
ISSN 2409–5613

DOI: 10.15826/chimtech.2019.6.3.03

A. A. Redkin[a], **S. V. Pershina**[a], **E. A. Il'ina**[a],
A. A. Kataev[a], **Yu. P. Zaikov**[a,b]
[a]*Institute of High-Temperature Electrochemistry of Ural Branch of RAS,*
20 Akademicheskaya St., 620137, Ekaterinburg, Russian Federation
[b]*Ural Federal University,*
19 Mira st., Ekaterinburg, 620002, Russian Federation
a.redkin@ihte.uran.ru

Heat of Fusion of Na_3AlF_6 Eutectic Mixtures with CaF_2 and Al_2O_3

The heat of fusion of eutectic mixtures of sodium cryolite with alumina and calcium fluoride was measured using differential scanning calorimetry. Melting temperatures were found to be in good agreement with literature data. The molar heat of fusion of cryolite salts and eutectic mixtures was found to be directly dependent on melting temperature. The temperature dependence coefficient is the same as that of alkali halides.

Keywords: heat of fusion; melting point; cryolite; heat balance; differential scanning calorimetry.

Received: 01.08.2019. Accepted: 11.10.2019. Published: 15.10.2019.

Introduction

Molten cryolites are applied as electrolytes in industrial production of aluminum due to high alumina solubility and high electrical conductivity [1]. However, it is difficult to use them due to their relatively high corrosion activity. One means of avoiding this issue is to create protective layer of frozen salts on the walls of electrolytic cell, but this layer, or ledge, is unstable due to high heat flows in the salt bath. In order to control the thickness of a side ledge, the knowledge of thermophysical properties of both liquid and frozen electrolyte is very important, as well as freezing and melting processes themselves. The heat that is absorbed or realized at melting or freezing is determined by the enthalpy of fusion. The main component of an aluminium bath is sodium cryolite, and its enthalpy of fusion was investigated by many researches. The very first results were very different from later data. Malinovsky [2] analyzed all results available in mid-eighties. His own results on heat of fusion were given as 115.4 $kJ\cdot mol^{-1}$ (considering cryolite as Na_3AlF_6) or 28.83 $kJ\cdot mol^{-1}$ (considering cryolite as 75 NaF — 25 AlF_3 in mol %.The data obtained by Malinovsky do not differ essentially from the previous ones [3, 4]. Latest results are also close to these data [5]. Along with sodium cryolite, the other cryolites were studied in works of Holm and Bjorge [3, 6].

The real bath consists not only of cryolite but also of the other components such as alumina and calcium fluoride. The composition of electrolyte is usually close to some eutectic mixture of sodium cryolite with alumina, calcium fluoride and aluminium fluoride plus some small quantities of initial components. Eutectic mixture behaviour at melting (freezing) is similar to that of individual substance, and it is possible to perform a precise measurement of the heat related to melting of such mixture. Heat of fusion measurements can be carried out by differential scanning calorimetry (DSC) and drop calorimetry. In drop calorimetry, the measured parameter is the enthalpy of the sample. The temperature dependence of enthalpy is discontinuous at a melting point. The difference between values for solid and liquid states is the heat of fusion. With the DSC method, the heat of fusion is calculated from the melting area.

The aim of the work was to measure the melting points and heats of fusion of some eutectic mixtures of cryolite with aluminium oxide and calcium fluoride. The measurements were carried out by DSC method, which can provide precise results.

Experimental

The chemicals used for the sample preparation are listed in Table 1. Aluminum fluoride was purified from oxygen containing admixtures by ammonium fluoride in a glassy carbon crucible. Part of NH_4F (10% of AlF_3) was placed on the bottom of the crucible, and the other part was mixed with aluminum fluoride in proportion as follows: 12 g of NH_4F per 100 g of AlF_3. The mixture was heated up to 723–773 K and kept for about 6 hours at that temperature. The reaction between aluminum oxide and ammonium fluoride is given below:

$$6NH_4F+Al_2O_3 = \\ = 2AlF_3+6NH_3+3H_2O \qquad (1)$$

The analysis on oxygen after purification had been made using LECO element analyzer (USA). The mass content of oxygen was less than 0.1%. The purity of other reagents was higher than 99.5% content of main component (Table 1); therefore, their purification was not required.

For preparation of cryolites with calcium fluoride and alumina, the aluminum fluoride was mixed with the other components of eutectic mixture, placed into platinum crucible and heated up to 1323 K. To avoid the oxidation, a small amount of NH_4F was added to the mixture. Ammonium fluoride was decomposed at 513 K and did not influence the composition of the mixture. After melting, the sample was poured into a graphite mould.

The investigations were carried out using a STA 449C Jupiter synchronous thermal analyzer (NETZSCH, Germany). The experimental setup ensures high accuracy of the measuring parameters: temperature (< 1 K); mass (± $1 \cdot 10^{-6}$ g); base line reproducibility (± 2.5 mW); enthalpy (± 3%). The apparatus was calibrated using pure

Table 1

Materials used in this work

Compound	Mass fraction purity, %	Supplier	Purification
NaF	99.5	Vecton	—
AlF_3	95	Vecton	Treatment by NH_4F
Al_2O_3	99.5	Achinsk alumina plant	—
CaF_2	99.5	Vecton	—

salts supplied by NETZSCH (CsCl, $AgSO_4$, $BaCO_3$, $RbNO_3$, $KClO_4$). Monocrystalline sapphire was used to calibrate the sensitivity. The measurements were performed under following conditions: temperature interval — 308–1300 K; heating rate — 10 K min^{-1}; atmosphere — pure argon; crucibles with lids — Pt–Rh. All measurements were carried out under the same conditions. All calculations were performed with NETZSCH Proteus software.

Results and discussion

Some eutectic compositions of cryolite with calcium fluoride and alumina were investigated; their compositions are given in Table 2.

The phase diagrams of these systems were widely studied and can be found in works [7–11]. The DSC curves are shown in Fig. 1. The weight loss was observed only after melting, and its value varied from 0.6 to 3%. There are some solid-solid transitions on the curves. The α–β cryolite solid transition is present in samples 1 and 4 (Figs. 1, *a, d*). The temperature of this transition is in good agreement with literature [12]. All curves containing calcium fluoride have endothermic peaks in the interval of 1060–1080 K.

Fedotieff and Iljinsky found two temperature halts in the cooling curves in this region for calcium fluoride containing compositions [7]. There are no α/β transitions of cryolite in samples 2 and 3. The transitions occur in mixtures which are quasi-binary such as Na_3AlF_6–Al_2O_3, Na_3AlF_6–AlF_3 and Na_3AlF_6–CaF_2. The sample 1 is such quasi-binary Na_3AlF_6–Al_2O_3 and sample 4 is close to quasi-binary Na_3AlF_6–CaF_2 due to the low concentration of alumina in this sample. The multi-component mixtures manifest other DSC peaks. Craig [9] investigated 8 eutectic mixtures of Na_3AlF_6–AlF_3–CaF_2–Al_2O_3. The lowest DSC peak temperature for these mixtures was found to be equal to 948 K. Melting peaks are very broad, but the same lines were observed by other scientists [8, 10].

Melting points of mixtures under investigation are in the interval of 1200–1220 K. It is in good agreement with the results presented in the article [11]. The values of melting points and heats of fusion are given in Table 3. The literature data on heats of fusion and melting points of cryolite salts are given in Table 4. Na_3AlF_6 is a coordination compound. Coordination compounds are inorganic salts formed by the combination of two or more simple compounds in stoichiometric ratio. In order to compare molar properties of coordination compounds and simple compounds, one must consider a coordination compound (in our case Na_3AlF_6) as a combination of simple

Table 2

The composition of samples under investigation

No	Composition/mass%				Composition/mol%			
	NaF	AlF_3	CaF_2	Al_2O_3	NaF	AlF_3	CaF_2	Al_2O_3
1	56.4	37.6	0.0	11.7	70.5	23.5	0.0	6.0
2	50.1	33.4	14.8	3.1	66.1	18.5	10.2	1.7
3	50.5	33.6	10.0	5.9	67.2	22.4	7.2	3.2
4	46.2	30.8	19.9	3.1	62.8	21.0	14.6	1.7

compounds, i.e. 3 molecules of NaF and 1 AlF_3. In order to to equalize cryolite with simple compounds its molecular weight must be given for 1 molecule (0.75 molecular weight of NaF and 0.25 molecular weight of AlF_3).

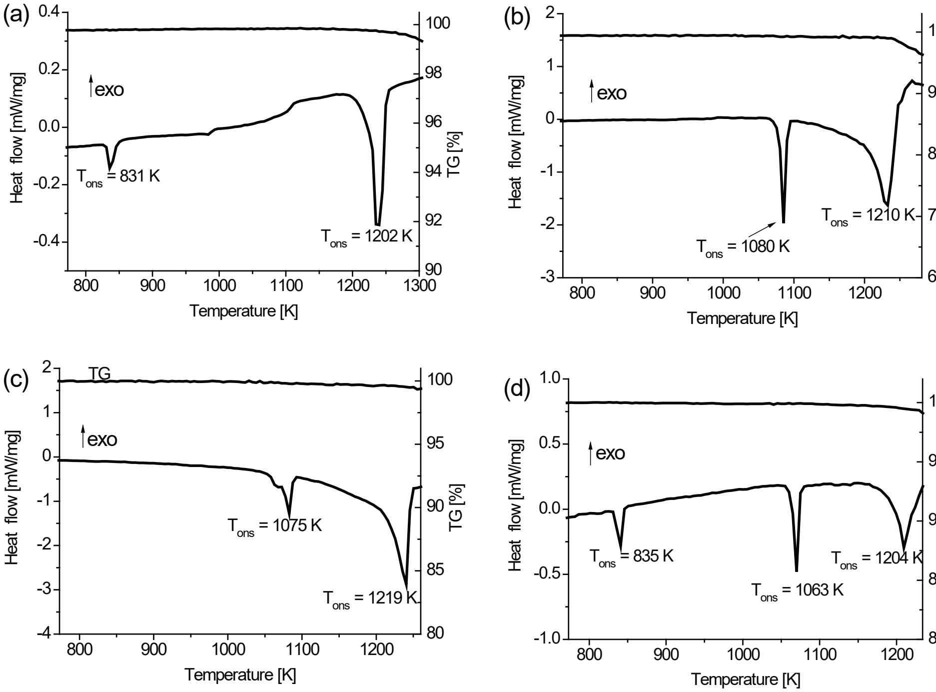

Fig. 1. DSC and thermogravimetric (TG) curves of cryolites with different composition: 1 (*a*), 2 (*b*), 3 (*c*), 4 (*d*) (see Table 2)

Table 3

Heats of fusion and melting points of eutectics under investigation

Comp. No	Transition point/K	ΔH_{tr}/ J g^{-1}	ΔH_{tr}/ kJ mol^{-1}	Melting point/K	ΔH_{m}/ J g^{-1}	ΔH_{m}/ kJ mol^{-1}
1	831	43.3	2.4	1202	476.6	26.4
2	1080	95.5	5.1	1210	501.8	26.6
3	1075	71.7	4.0	1219	477.2	26.7
4	835	44.2	2.5	1204	455	26.0
	1063	84.3	4.8	—	—	—

Table 4

Heats of fusion and melting points of cryolites

Compound	T_{mp}/K	H_{fus}/kJ mol^{-1}	Compound	T_{mp}/K	H_{fus}/kJ mol^{-1}
Li_3AlF_6	1058 [4]	21.0 [4]	Na_3AlF_6	1284 [2]	28.3 [2]
Li_3AlF_6	1058 [2]	22.0 [2]	Na_3AlF_6	1284 [1]	28.9 [1]
Na_3AlF_6	1284 [3]	28.8 [3]	K_3AlF_6	1273 [2]	30.8 [2]

Thus, the literature data were recalculated using the molecular mass of mixture as a sum of 75% of molecular mass of alkali halide and 25% of molecular mass of aluminium fluoride. It allows comparing results with data on individual salts. All the results are presented in Fig. 2 in coordinates as follows: heat of fusion — melting point.

There is a clear correlation between the enthalpy of melting and the melting point. The nature of this correlation is in thermodynamics, because

$$T_m=\Delta H_m/\Delta S_m, \qquad (2)$$

where T_m is the melting temperature, ΔH_m is the enthalpy of fusion, and ΔS_m is the entropy of fusion.

The correlation between the enthalpy of melting and the melting point for alkali halide salts was found in our previous article [13]. The same correlation was shown for nitrates, carbonates and sulphates [14]. This trend is the part of more broad relationship known as Trouton's rule, which connect enthalpy of phase transition with its temperature. It is valid both for vaporization of pure elements [15] and for melting [16, 17].

According to LSM (least-squares method) estimations, the coefficients in the equation $H = A+B\cdot T$ are as follows: B_{SQ} = 0.034 kJ mol^{-1} K^{-1}; A_{SQ} = −14.25 kJ mol^{-1}; T — temperature, K. The standard deviation σ_{SQ} is equal to 0.815 kJ mol^{-1}, and the determination coefficient R^2=0.94.

Thus, the equation is:

$$\Delta H_m/\text{kJ mol}^{-1} = \\ =B_{SQ}\cdot T_m - A_{SQ} = 0.034\ T_m - 14.25 \qquad (3)$$

Table 5

The values of coefficients in equations for heat of fusion dependence on the melting point

Compounds	Parameter A_{SQ}/kJ mol^{-1}	Parameter B_{SQ}/kJ mol^{-1} K^{-1}
Cryolites	−14.25	0.034
Alkali halides [7]	−12.12	0.036

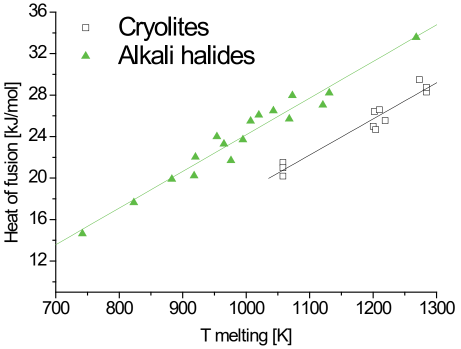

Fig. 2. Heat of fusion dependence on the melting point for cryolites and alkali halides

The heat of fusion temperature coefficient of cryolites is close to that of alkali halides. Thus, the temperature dependence of heat of fusion is the same for halide compounds and equal to the value for alkali halide salts. The values of temperature coefficients are close to 4*R*. It is the same number as heat capacity of halide salts per atom [18].

Thus, the heat of fusion is directly proportional to the melting point for simple halide salts, salts compounds and eutectic mixtures. The fusion properties of all these substances are possibly connected due to the fact that the main components of these compounds are halide salts.

Conclusions

1. Heats of fusion were measured for some eutectic mixtures of sodium cryolite with alumina and calcium cryolite.

2. The heat of fusion was found to be directly proportional to the melting point.

Acknowledgements

The work was supported by RFBR. Grants No 18-03-00785 A.

The authors are grateful to O. Reznitskikh from Solid State Chemistry Institute of Ural Branch of RAS for useful contribution to the work.

References

1. Fellner P, Haarberg GM, Híves J, Kvande H, Sterten A. Aluminium Electrolysis. Fundamentals of the Hall-Héroult Process. Aluminium Verlag: Dusseldorf; 2001. 443 p.
2. Malinovsky M. Cryometric determination of the enthalpy of fusion of sodium cryolite. Chem Zvesty. 1984;38(2):168–72.
3. Holm B, Gronvold F. Enthalpies of fusion of alkali cryolites determined by drop calorimetry. Acta Chem Scand. 1973;27:2043–50. DOI: 10.3891/acta.chem.scand.27–2043.
4. O'Brien C, Kelley K. High temperature heat content of cryolite, anhydrous aluminium fluoride and sodium fluoride. J Amer Chem Soc. 1957;79:5616–18. DOI: 10.1021/ja01578a009.
5. Dolejs D, Baker D. Phase transitions and volumetric properties of cryolite, Na_3AlF_6: Differential thermal analysis to 100 MPa. Am Mineral. 2006;91:97–103. DOI: 10.2138/am.2006.1772.
6. Bjorge B, Jenssen B. The calorimetric heat of fusion of Li_3AlF_6. Acta Chem Scand. 1968;22:1347–48. DOI: 10.3891/acta.chem.scand.22–1347.
7. Fedotieff PP, Iljinsky WP. Uber die Smellzbarkeit des ternaren Systems: Natriumfluorid, Calciumfluorid, Aluminium Fluorid. Z fur Anorg. und Allgem. Chemie. 1923;129:93–107.
8. Holm J. The phase diagram of the system Na_3AlF_6-CaF_2 and the constitution of the melt in the system. Acta Chem Scand. 1968;22:1004–12. DOI: 10.3891/acta.chem.scand.22–1004.
9. Craig D, Brown J. Phase equilibria in the system CaF_2–AlF_3–Na_3AlF_6 and part of the system CaF_2–AlF_3–Na_3AlF_6–Al_2O_3. J Am Ceramic Soc. 1980;63:254–61. DOI: 10.1111/j.1151–2916.1980.tb10714.x.
10. Tissot **P.** DTA determination of liquidus temperatures and Al_2O_3 and AlF_3 content in cryolitic melts. Thermochim Acta. 1994;234:245–54. DOI: 10.1016/0040–6031(94)85147–6.
11. Fenerty A, Hollingshead E. Liquidus curves for aluminum cell electrolyte: III. Systems Cryolite-Alumina with Aluminum Fluoride and Calcium Fluoride. J Electrochem Soc. 1960;107:993–97. DOI: 10.1149/1.2427588.
12. Gheribi A, Salanne M, Chartrand P. Formulation of Temperature-Dependent Thermal Conductivity of NaF, β-Na_3AlF_6, $Na_5Al_3F_{14}$, and Molten Na_3AlF_6 Supported by Equilibrium Molecular Dynamics and Density Functional Theory. J Phys Chem C. 2016;120(40):22873–86. DOI: 10.1021/acs.jpcc.6b07959.

13. Redkin A, Korzun I, Reznitskikh O, Yaroslavtseva T, Zaikov Yu, Kumkov S. Heat of fusion of halide salts and their eutectics. J Therm Anal Calorim. 2018;131:2021–26. DOI: 10.1007/s10973-017-6650-4.
14. Badenhorst H, Bohmer T. Enthalpy of fusion prediction for the economic optimisation of salt based latent heat thermal energy stores. Journal of Energy Storage. 2018;20:459–72. DOI: 10.1016/j.est.2018.10.020.
15. Wisniak J. Frederick Thomas Trouton: The man, the Rule and the Ratio. J Chem Educator. 2001;6:55–61. DOI: 10.1007/s00897000448a.
16. Sawamura H. The relation between entropy of fusion or heat of fusion of metallic elements and their crystal structure. Trans JIM. 1972;13:225–30. DOI: 10.2320/matertrans1960.13.225.
17. Kaptay G. On the solid/liquid interfacial energies of metals and alloys. J. Mat. Sci. 2018;53: 3767–84. DOI: 10.1007/s10853-017-1778-y.
18. Redkin A, Zaikov Y, Korzun I, Reznitskikh O, Yaroslavtseva T, Kumkov S. Heat capacity of molten halides. J Phys Chem B. 2015;119:509–12. DOI: 10.1021/jp509932e.

Please note that all new submissions will be accepted in English only. Requirements for the manuscript preparation are available on the Journal's website and in the following template

Chimica Techno Acta manusctipt style guidelines (title)

A.N. Authorname[a], A.N. Authorname[b], A.N. Authorname[ab]
[a] Institution, address, city, country
[b] Institution, address, city, country
e-mail: corresponding_author@e-mail.com

Abstract

The abstract should be a single paragraph (up to 300 words) in plain text (that means — no formulae or references are permitted) that summarises the content of the article. It should set the main objectives and results of the work; giving the reader a clear idea of what has been achieved. An abstract should not be extremely short though — if yours is 1–2 sentences long, then you’re not doing it right. Make sure that you use well-known, searchable terms and phrases.

Keywords: short; searchable; keywords (up to 10).

Introduction

An introduction should ‘set the scene’ of the work. It should clearly explain both the nature of the problem under investigation and its background. It should start off general and then focus in to the specific research question you are investigating. Ensure you include all relevant references.

Experimental (if appropiate)

Descriptions of the experiments should be provided in enough detail so that a skilled researcher is able to repeat them. Methods already published or experimental techniques already described elsewhere should be indicated by a reference. Only non-standard apparatus should be described in details; commercially available instruments are referred to by their stock numbers.

Results and discussion

This is undoubtedly the most important section of your article. It should consist of the logically ordered sequence of text, formulae, images and tables.

All formulae which appear in their own line should be numbered:

$$A = B + C \tag{1}$$

Tables should be used only when they can present information more efficiently than running text or even an image:

Table 1

Just an ordinary table without any sophisticated formatting applied

A	B	C	D
1	2	3	4
+	+	+	–

All illustrations should be of a high quality (300 dpi or higher) and should be placed in the flow of the text, not in the end of an article:

Fig. 1. Just an ordinary image

Please bear in mind that all illustrations and tables should fit smoothly within either single column (approx. 6 cm) or double column (approx. 12 cm) width.

Conclusions

Your conclusions should summarize the main paper, underline the interpretation of the key results and highlight the novelty and significance of the work. They may address some plans for relevant future work as well.

Acknowledgements (if appropiate)

All sources of funding such as grants should be declared here. Individuals who contributed to the research but are not co-authors may also be briefly acknowledged.

References

A reference should be indicated in square brackets in line with the text (e.g. [1]). The actual references in the reference list should be numbered in the order in which they appear in the text. In Chimica Techno Acta so-called Vancouver Citation Style is adopted almost as it is described in the following public domain textbook [1]:

1. Patrias K. Citing medicine: the NLM style guide for authors, editors, and publishers [Internet]. 2nd ed. Wendling DL, technical editor. Bethesda (MD): National Library of Medicine (US); 2007- [updated 2015 Oct 2; cited 2017 Jun 07]. Available from: http://www.nlm.nih.gov/citingmedicine

Note that opposed to [1] we omit the date of publication (leaving year only) of the referenced journal article, as almost all journals are continuously paginated throughout the volume. And another one — DOI or a hyperlink should always come last in a reference. These are the only major differences between our style and such described in [1], so when in doubt — you can always refer to [1], it contains tremendous number of well-organized examples.

For your convenience, below are some references to the different types of publications:

Books

2. Livingstone S. The Chemistry of Ruthenium, Rhodium, Palladium, Osmium, Iridium and Platinum. Oxford: Pergamon; 1973. 222 p.

3. Bard AJ, Faulkner LR. Electrochemical Methods: Fundamentals and Applications. 2nd ed. New York: John Wiley & Sons; 2001. 833 p.

Books not in English

4. Evdokimov AA, Efremov VA, Trunov VK, Kleyman IA, Tananaev IV. Soedineniya redkozemel'nykh elementov. Molibdaty, vol'framaty [Rare-earth elements' compounds. Molibdates, wolframates]. Moscow: Nauka; 1991. 267 p. Russian.

* Translation of the title in square brackets is not required, but highly desirable.

* For Cyrillic languages, such as Russian, please use consistent transliteration system. There are plenty, but we strongly recommend BGN/PCGN Romanization as it's one of the

easiest to read and implement (https://en.wikipedia.org/wiki/BGN/PCGN_romanization_of_Russian).

Journal articles

5. Zuev AYu, Tsvetkov DS. Oxygen nonstoichiometry, defect structure and defect-induced expansion of undoped perovskite LaMnO$_{3\pm\delta}$. Solid State Ionics. 2010;81(11–12):557–63. DOI:10.1016/j.ssi.2010.02.024

6. Shannon RD. Revised effective ionic radii and systematic studies of interatomic distances in halides and chalcogenides. Acta Cryst. 1976;A32:751–67. DOI:10.1107/S0567739476001551

7. Allred AL, Rochow EG. A scale of electronegativity based on electrostatic force. J Inorg Nucl Chem. 1958;5(4):264–8. DOI:10.1016/0022-1902(58)80003-2

* For the majority of chemical journals corresponding abbreviation is defined in Chemical Abstracts Service Source Index (CASSI, http://cassi.cas.org). If an abbreviation is not available there, please use the full name of a journal.

* Note that DOI of an article, when available, should always be provided.

Journal articles on the Internet (e.g. for online-only journals without DOI)

8. Tkach V, Nechyporuk V, Yagodynets P. Descripción matemática de la síntesis electroquímica de polímeros conductores en la presencia de surfactants. Avances en Química [Internet]. 2013[cited 2016];8(1):9–15. Spanish. Available from: http://erevistas.saber.ula.ve/index.php/avancesenquimica/article/download/6357/6168

Conference abstracts

9. Zuev AYu, Sereda VV, Malyshkin DA, Ivanov IL, Tsvetkov DS. Mechano-chemical coupling in double perovskites as energy related materials. In: Abstracts of the XX Mendeleev Congress on general and applied chemistry, Vol. 3; 2016 Sep 26–30; Ekaterinburg, Russia. p. 325.

10. Steparuk AS, Usachev SA, Tsvetkov DS, Sosnovskikh VYa, Zuev AYu. Novyy katodnyy material na osnove mayenita dlya elektrokhimicheskogo karboksilirovaniya organicheskikh soedineniy [New mayenite-based cathode material for electrochemical carboxylation of organic compounds]. In: Tezisy dokladov XXVI Rossiyskoy molodezhnoy nauchnoy konferentsii “Problemy teoreticheskoy i eksperimental’noy khimii” [Abstracts of XXVI Russian scientific conference for young scientists “Problems of theoretical and experimental chemistry”]; 2016 Apr 27–29; Ekaterinburg, Russia. p. 285–286. Russian.

Dissertations

11. ten Donkelaar SFP. Development of Stable Oxygen Transport Membranes [dissertation]. Enschede (The Netherlands): University of Twente; 2015. 140 p.

Patents

12. Chemezov OV, Batukhtin VP, Apisarov AP, Isakov AV, Zaikov YuP, inventors; Institute of High-Temperature Electrochemistry UB RAS, assignee. Sposob polucheniya nano- i mikrovolokon kremniya elektrolizom dioksida kremniya iz rasplavov soley. Russian Federation patent RU 2427526. 2011 Aug 27. Russian.

13. Menta E, Da Re G, Grugni M., authors; Cti Europe S.R.L., assignee. Derivatives of chromen-2-one as inhibitors of vegf production in mammalian cells. United States patent US20060122387 A1. 2006 Jun 8.

Учредитель —
Уральский федеральный университет
имени первого Президента России Б. Н. Ельцина
620002, Россия, Екатеринбург, ул. Мира, 19

Свидетельство о регистрации
ПИ № ФС77-56172 от 15.11.2013

Адрес журнала:
Россия, 620000,
Екатеринбург, ул. Мира, 28, оф. Х-268
E-mail: t.a.pospelova@urfu.ru

Формат 70×100/16. Тираж 500 экз. Заказ № 320.

Отпечатано в типографии
Издательско-полиграфического центра УрФУ
620000, Екатеринбург, ул. Тургенева, 4
Тел.: +7 (343) 350-56-64, 350-90-13
Факс: +7 (343) 358-93-06
E-mail: press-urfu@mail.ru

Chimica Techno Acta

Founded by Ural Federal University named after
the first President of Russia B. N. Yeltsin
19, Mira St., Ekaterinburg, 620002, Russia

Journal Registration Certificate
PI № FS 77-56172 as of 15.11.2013

Principal Contact
Office X-268, Mira Str.,
620000, Ekaterinburg, Russia
E-mail: t.a.pospelova@urfu.ru

Format 70×100/16.
Circulation 500 cop.

Publisher — Ural Federal University
Publishing Centre
4, Turgenev St., 620000 Ekaterinburg, Russia
Phone: +7 343 350 56 64, +7 343 350 90 13
Fax: +7 343 358 93 06
E-mail: press-urfu@mail.ru